CNWRA A center of excellence in earth sciences and engineering ™

A Division of Southwest Research Institute®
6220 Culebra Road • San Antonio, Texas, U.S.A. 78228-5166
(210) 522-5160 • Fax (210) 522-5155

June 4, 2004
Contract No. NRC–02–02–012
Account No. 06002.01.051

U.S. Nuclear Regulatory Commission
ATTN: Dr. John S. Trapp
Office of Nuclear Material Safety and Safeguards
Two White Flint North, Mail Stop 7 D13
Washington, DC 20555-0001

Subject: Completion of Intermediate Milestone—Magma Flow Through Elastic-Walled Dikes (IM 06002.01.051.471)

Dear Dr. Trapp:

Attached is IM 06002.01.051.471, "Magma Flow Through Elastic-Walled Dikes," which was originally titled "Magma-Repository Investigations—Journal Article" in Fiscal Year 2004 Operations Plans. This report presents a first-order numerical model to evaluate the likely relationships between wall-rock stress and magma flow processes. The numerical model is developed using convective-diffusive flow relationships, which are coupled to elastic wall-rock responses to stress. Using a finite element discretization, different flow conditions are evaluated to determine stationary and traveling-wave solutions for the model. These solutions are used to describe the physical conditions of incompressible magma flow in subvolcanic conduits, which account for linkages between magma pressure and wall-rock stress. The model is applied to eruptions at Tolbachik and Montserrat volcanoes, and found to reasonably represent observed magma-flow conditions.

This numerical model for convective-diffusive magma flow represents a different conceptual approach than used recently in Woods, et al. (2004) (IM 06002.01.051.320). The Woods, et al. (2004) model evaluates steady-state flow conditions using relationships for conservation of mass and momentum in fluid systems. By assuming steady-state conditions, the Woods, et al. (2004) model can evaluate compressibility effects on flow resulting from volcanic gasses. In contrast, the current model evaluates dynamic flow conditions. Although the complexity of the current model does not permit evaluation of compressibility effects, this model provides useful insights on transient conditions that appear relevant to evaluating the dynamics of potential magma-repository interaction processes. In addition, the current model provides similar results as the Woods, et al. (2004) model for steady-state incompressible flow conditions.
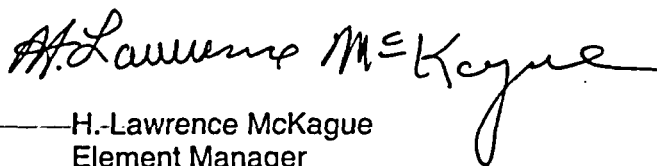
Washington Office • Twinbrook Metro Plaza #210
12300 Twinbrook Parkway • Rockville, Maryland 20852-1606

Initial models for potential magma flow into a subsurface drift (Woods, et al., 2002) assumed instantaneous opening of the dike and no feedback between wall-rock stress and magma flow rate. The current work was undertaken to better understand how elastic deformation of the wall rock may influence magma flow rates in an ambient stress field. The models in this report, however, are not directly applied to potential igneous events at Yucca Mountain, Nevada. Staff are working with consultants to apply the models in this report to the specific subsurface conditions of Yucca Mountain, and directly evaluate potential magma-repository interaction processes. Results of these applications are planned for discussion at the July, 2004, workshop on potential magma-repository interaction processes.

Following NRC review and acceptance of this report, staff plans to submit this report to the journal, *Theoretical and Computational Fluid Dynamics*, for publication. Thus, the report is formatted following this journal's requirements. If you have any questions, please contact Dr. Brittain Hill at 210-522-6087 or me at 210-522-5183.

<div align="center">Sincerely,</div>

<div align="center">H.-Lawrence McKague
Element Manager</div>

/slo
Enclosures

cc:			
B. Meehan	E. Collins	A. Campbell	W. Patrick
W. Reamer	L. Kokajko	P. Justus	B. Hill
D. DeMarco	F. Brown	B. Leslie	D. Hooper
E. Whitt	K. Stablein	J. Rubenstone	R. Benke
W. Ford	M. Bailey	R. Codell	CNWRA Dirs/EMs (letter only)
T. McCartin	L. Campbell	K. Compton	L. Gutierrez (letter only)
			Record Copy B, IQS

Magma Flow through Elastic-Walled Dikes

O. Bokhove[1], A.W. Woods[2], and A. de Boer[1]

1. Deartment of Applied Mathematics, University of Twente, The Netherlands
2. BP Institute for Multiphase Flow, University of Cambridge, U.K.

May 18, 2004

Abstract

A convection-diffusion model for the averaged flow of a viscous, incompressible magma through an elastic medium is considered. The magma flows through a dike from a magma reservoir to the Earth's surface; only changes in dike width and velocity over large vertical length scales relative to the characteristic dike width are considered. The model emerges when nonlinear inertia terms in the momentum equation are neglected in a viscous, low-speed approximation of a magma flow model coupled to elastic waves in rock.

Stationary- and traveling-wave solutions are presented in which a Dirichlet condition is used at the magma chamber; and either a (i) free boundary condition, (ii) Dirichlet condition, or (iii) choked-flow condition at the moving free- or fixed-top boundary. A choked-flow boundary condition, generally used in the coupled elastic wave and magma flow model, is also used in the convection-diffusion model. The validity of this choked-flow condition is illustrated by comparing stationary flow solutions of the convection-diffusion and coupled elastic wave and magma flow model for parameter values estimated for the Tolbachik volcano region in Kamchatka, Russia. These free- and fixed-boundary solutions are subsequently used in the numerical verification and validation of a novel extension of a conservative, local discontinuous Galerkin finite-element discretization. The method uses a mixed Eulerian-Lagrangian finite element near the free boundary and ensures positivity of the mean aperture subject to a timestep restriction. A simulation of magma flow with quasi-periodic growth and collapse of a lava dome based on parameter estimates for the Soufrière Hills Volcano on Montserrat illustrates the meaning of the model and its analysis.

1   Introduction

We consider the dynamics of viscous, incompressible magma through a dike surrounded by host rock. The dike runs from a magma reservoir deep in the rock to

the Earth's surface. At leading order, the rock is modeled as an elastic medium in which the dike width is approximated to be proportional to the difference in fluid pressure and the lithostatic pressure caused by the overlying weight of the rock. In this relation, the anisotropy of the stresses is explicitly included by assuming the least principal stress to be horizontal. When changes of the flow over large vertical scales relative to the width or cross section of the aperture are considered, the flow across the aperture is locally in viscous equilibrium. For simplicity, we assume the viscosity to be constant. Hence, the mass and momentum equations averaged over this cross section yield a convection-diffusion equation after inertia terms in the momentum equation have been neglected. The resulting model equals the fracture-propagation model of Pinel and Jaupart (2000) for the limit of isotropic stresses in the rock once the influence of an edifice load at the surface is neglected. In contrast, our simplified model is still (asymptotically) valid for small edifice loads and is more amenable to mathematical analysis.

In particular, stationary and traveling-wave solutions are derived for the convection-diffusion model, either analytically or by numerically solving the relevant ordinary-differential equations. Solutions are derived for both a free- and fixed-top boundary; the first describing magma driving its way along a preexisting crack to the surface, and the latter describing the magma flow for (time-dependent) pressure conditions at the surface. In both cases, the (time-dependent) pressure condition at the magma chamber is prescribed. For high velocities, inertial terms become important, and a momentum and a continuity equation describe the leading-order flow in an elastic dike. The most appropriate boundary condition at the top appears to be the condition of choked or critical flow at the surface. The speed of the flow then matches the velocity of the elastic waves. Despite the lack of inertial terms, the condition of criticality at the top also seems appropriate for the convection-diffusion equation: it could be viewed as the outcome of an analysis in a boundary layer near the surface of the inertial, elastic-flow equations. Steady-flow solutions aiming to represent an eruption of the Tolbachik volcano region in Kamchatka, Russia, show that the solutions of both models are nearly equal when the flow is enforced to be critical at the top (cf. the inertial, elastic-flow solutions in Woods et al., 2004).

These high-resolution exact and numerical solutions are subsequently used to verify a novel application and extension of a conservative, local discontinuous Galerkin finite-element method for convection-diffusion equations (building on Cockburn and Shu, 1998). First, the extended numerical approach uses an upwind flux to ensure positivity of the mean aperture subject to a timestep restriction and is additionally designed to satisfy L_2-stability for suitable boundary conditions. Second, the asymptotic solution at the free boundary or front is used as a basis function in the time-dependent free-boundary element because the solution at this free boundary is singular and can, therefore, not be matched easily and satisfactorily in any numerical method and by the usual polynomial basis and test functions in discontinuous

Galerkin methods in particular. The free-boundary treatment uses fixed Eulerian elements away from the free boundary and a mixed Eulerian-Lagrangian element at the free boundary akin to the flooding and drying approach in Bokhove (2004). Although in one dimension an entirely Lagrangian treatment is feasible, the presented mixed Eulerian-Lagrangian elements are better suited for extension to two-dimensional flow through a magma dike averaged only over its narrow width. The consideration of such two-dimensional flows through a dike instead of a (nearly) symmetric flow through a horizontally uniform dike is important for applications in which the influence of local sources and sinks of magma in a dike needs to be investigated. Such evolving asymmetric flows in a dike can occur because of heterogeneities in the surrounding host rock (near the free surface), horizontal pressure distributions in the magma chamber, or existing subsurface tunnels intersected by a rising magmatic dike.

Verification of the numerical approach is performed by a comparison with the high-resolution, stationary and traveling-wave solutions for both the free- and fixed-boundary cases. Finally, validation of the model is performed while simulating the growth of a lava dome, caused by magma flow through a dike arising from a chamber, and its collapse when a critical height has been reached. Parameter values are roughly based on the Soufrière Hills Volcano on Montserrat.

The organization of this paper is as follows: the convection-diffusion model is introduced in section 2 and the numerical approach is developed in section 3 and Appendix A. Stationary and traveling-wave solutions are derived in section 4.1, and a numerical verification and validation is provided in section 4.2 and section 4.3. Finally, the conclusion is in section 5.

2 Elastic Wall-Fluid Equations

We investigate the flow of an incompressible fluid with a constant density, ρ_m, through a vertical aperture of variable width, b. The aperture, b, is narrow enough, relative to the vertical scales being considered, that we consider only the averaged velocity, u, along the vertical. In that case, the flow profile at each cross section is assumed to be close to its viscous equilibrium even though we allow smooth and sufficiently slow variations in the vertical and in time. The averaged mass and momentum equations are

$$\partial_t(\rho_m\, b) + \partial_z(\rho_m\, b\, u) = 0 \qquad (2.1a)$$

$$\partial_t(\rho_m\, u) + u\, \partial_z(\rho_m\, u) = -\partial_z p - \rho_m\, g - \gamma\, \mu\, u/b^2 \qquad (2.1b)$$

with time t; vertical coordinate z; magma pressure p; gravitational acceleration g; and viscosity μ. The last, frictional term in (2.1b) matches the friction of an incompressible flow assumed to be in local equilibrium. For a slit, $\gamma = 12$. These frictional coefficients follow from considering steady, viscous flow in a planar configuration.

3

The system is closed by relating the aperture, b, to the pressure in the fluid and the pressure in the solid at the wall.

In the geophysical application considered, the medium around the aperture is the host rock. The aperture, b, is then proportional to the difference in the fluid, p, and wall pressure, p_r. A sketch of the configuration is provided in Fig. 1a. Assuming an elastic response of the rock surrounding the aperture (cf., Pinel and Jaupart, 2000), we take

$$b = \begin{cases} \lambda \left(p - \kappa p_r \right) & \text{if } p \geq \kappa p_r \\ 0 & \text{if } p < \kappa p_r \end{cases} \tag{2.2}$$

with λ describing the elasticity of the host medium. This elastic response is valid when the aspect ratio between horizontal and vertical length scales, and the aspect ratio, a/b, of the semi-axes of a thin elliptical fracture are (asymptotically) small. The parameter, $0 < \kappa \leq 1$, is introduced because the pressure in the rock does not have to be isotropic, which means the horizontal stresses, which cause the opening or closing of the dike, can be smaller than the vertical one, and κ will denote the ratio between the horizontal and the vertical stresses. We assume p_r to be in lithostatic balance

$$\partial_z p_r = -\rho_r\, g \tag{2.3}$$

with $\rho_r = \rho_r(z)$ the density of the rock.

Hence, from (2.1a)–(2.1b) and (2.3), we obtain

$$\partial_t b + \partial_z (b\, u) = 0$$
$$\partial_t u + u\, \partial_z u = -\frac{1}{\rho_m\, \lambda} \partial_z b + (\kappa\, \rho_r - \rho_m)\, g/\rho_m - \gamma\, \mu\, u/\rho_m b^2. \tag{2.4}$$

It is a system that supports elastic waves with speed $c_e = \sqrt{b/(\rho_m\, \lambda)}$ (see, e.g., Whitham, 1974). The flow of magma in the dike is generally subcritical with $0 < u \leq c_e$, except at the Earth's surface where it is generally modeled to be critical (i.e., with $u = c_e$).

2.1 Elastic Convection-Diffusion Equations

When the flow is viscously dominated, we can ignore the inertia term on the left-hand side of the momentum equation, (2.1b) or (2.4) and use (2.2) and (2.3) to obtain

$$u = -\frac{b^2}{\gamma\, \mu\, \lambda} \partial_z b + \frac{g\, b^2}{\gamma\, \mu} (\kappa\, \rho_r - \rho_m) \tag{2.5}$$

with ρ_m constant but with $\rho_r = \rho_r(z)$ the variable density of the host rock. After combining (2.5) with the mass equation, (2.1a), we arrive at the following convection-diffusion equation

$$\partial_t b + \partial_z (\alpha\, b^3 - \beta\, b^3\, \partial_z b) = 0 \tag{2.6}$$
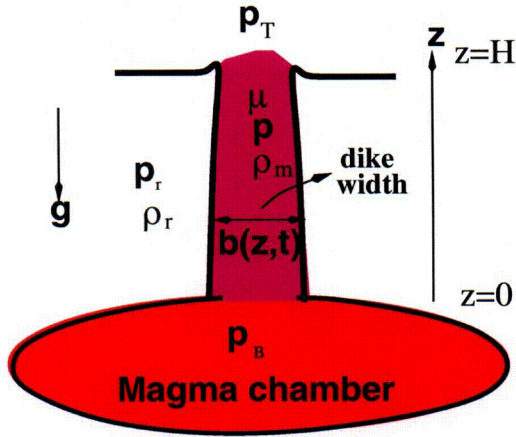
4

Figure 1: Configuration sketch of the geophysical application with a magma chamber, dike of aperture, $b(z)$, and lava dome. The ambient pressure, p_T, is atmospheric.

with the dimensional expressions for $\alpha = \alpha(z)$ and nonnegative β given by

$$\alpha(z) = g\left[\kappa\,\rho_r(z) - \rho_m\right]/(\gamma\,\mu) \qquad \text{and} \qquad \beta = 1/(\gamma\,\mu\,\lambda) \geq 0. \tag{2.7}$$

This convection-diffusion equation is essentially equivalent to the the fracture propagation model of Pinel and Jaupart [2000, their equation (4.11)] when the edifice load caused by the weight of a lava dome above a preexisting crack in their model is considered sufficiently (or asymptotically) small and, hence, is ignored. The elasticity of the medium is then $\lambda = a\,(1-\nu)/G$ for a dike or fracture of elliptical cross section with $G \approx 1.125\,10^9\,Pa$ as the rigidity, $\nu \approx 0.25$ as Poisson's ratio, and $a \approx 100\,m$ as the long semi-axis of the elliptical crack (cf., Pinel and Jaupart, 2000). To ignore the edifice load, the appropriate asymptotic number is the aspect ratio of the height of the lava dome versus the depth of the dike. For a lava dome height of $h_v = 100 - 1000\,m$ and a total conduit depth of $H = 3 - 10\,km$, this ratio lies between 0.01 and 0.333. Pinel and Jaupart (2000) considered the case in which the ratio of the semi-axes of the ellipse is $1:100$, which results in the symmetric dike model used presently.

After scaling the convection-diffusion equation (2.6) using $b = D_0\,b'$, $t = T_0\,t'$, $z = H_0\,z'$, $H = H_0\,H'$, and $T_0 = \gamma\,\mu\,\lambda\,H_0^2/D_0^3$ and dropping the primes, we find (2.6) with (dimensionless) $\beta = 1$ and $\alpha(z) = g\left[\kappa\,\rho_r(z) - \rho_m\right]\lambda\,H_0/D_0$. Typical variables are provided in Table 1 which results in a range $\alpha = (-25, 50)$ with typically $\alpha \approx (0.1, 1)$.

We assume that $u \geq 0$ so the boundary at $z = 0$ is an inflow boundary. The dimensionless flow domain, $\Omega_f \subseteq \Omega = \{z \in (0, H)\}$, provided $b(z, t) > 0$ and may be smaller when the dike is closed so $b = 0$. We consider the following combinations of boundary conditions. (i) The pressures at the magma chamber and the exit, and

5

Variable	Value	Unit
g	9.81	m/s^2
κ	0.95	–
ρ_r	$2,500 - 2,900$	kg/m^3
ρ_m	$2,500$	kg/m^3
λ	$10^{-8} - 10^{-6}$	$m^2\,s^2/kg$
D_0 (dike)	$0.5 - 2$	m
D_0 (conduit)	$5 - 10$	m
H_0	$1 - 10$	km
α (dike)	$(-25, 50)$	–

Table 1: Typical values of the variables introduced.

hence the bottom and top width, are specified yielding Dirichlet boundary conditions, $b(0,t) = b_B(t)$ and $b(H,t) = b_T(t)$. (ii) The pressure at the magma chamber is specified, $b(0,t) = b_B(t)$, and the flow at the exit is critical

$$u(H,t) = \sqrt{b_T/(\rho_m\,\lambda)} \quad \text{(dimensional) or} \quad u(H,t) = \gamma_c\sqrt{b} \quad \text{(dimensionless)} \quad (2.8)$$

with $\gamma_c = \sqrt{\lambda/\rho_m}\,\gamma\,\mu\,H_0/D_0^{5/2}$. (iii) The pressure at the magma chamber is specified, $b(0,t) = b_B(t)$, and there is a free boundary at $z = z_r(t) < H$ where $b(z_r(t),t) = 0$. At the free boundary

$$dz_r(t)/dt = u_r(t) = u(z_r(t),t) = -\beta\lim_{b\downarrow 0}(b^2\,\partial_z b). \quad (2.9)$$

The free boundary in case (iii) will evolve into case (i) or (ii) when it reaches the exit. This exit position at $z = H(t)$ may be time dependent when a lava dome is growing or collapsing. As initial condition, we have $b(z,0) = b_i(z)$.

Next, we investigate what happens at such a free boundary. A front at $z = z_r(t)$ may exist where the aperture, $b = 0$, with $b > 0$ for an interval, $0 < z < z_r(t)$. When $b \downarrow 0$ as $z \uparrow z_r(t)$, the velocity limits to

$$\lim_{b\downarrow 0} u = \lim_{b\downarrow 0}(\alpha\,b^2 - \beta\,b^2\,\partial_z b) = u_r(t). \quad (2.10)$$

Because the velocity, u, must be finite, the slope of the aperture at the front has to be infinite or vertical. The solution Ansatz at the front is that $b = D_0\,[z_r(t) - z]^{1/3}$ with $D_0 = D_0(t)$ constant in space, giving a finite frontal velocity, $u_r(t)$. Alternatively, consider a boundary layer with scaled coordinate, $\eta = (z_r - z)/\epsilon$, and time, $\tau = t/\epsilon$, with $\epsilon \ll 1$. Applying this change of coordinates in (2.6), expanding $b = b^{(0)} + \epsilon\,b^{(1)} +$

$O(\epsilon^2)$, and evaluating at leading order $1/\epsilon^2$ yields

$$\partial_\eta b^{(0)} \frac{dz_\tau}{d\tau} = \beta\, \partial_\eta[b^{(0)^3} \partial_\eta b^{(0)}]. \tag{2.11}$$

Integration over η gives

$$b^{(0)} \frac{dz_\tau}{d\tau} - Q_f = \beta\, b^{(0)^3} \partial_\eta b^{(0)}. \tag{2.12}$$

If $Q_f \neq 0$, the discharge, $u\,b$, is finite at the front. The velocity, u, is then infinite at and large near the front, which is unphysical and mathematically inconsistent. In the derivation of the advection-diffusion model, the inertia terms were considered negligible in the momentum equation, (2.1b), but for large velocities these terms should be included. Hence, we have to consider $Q_f = 0$ to be consistent. Further integration of (2.12) yields the free-boundary condition and the asymptotic aperture profile at the front:

$$dz_\tau/dt = u_r(t) = \frac{1}{3}\beta\, D_0^3 \qquad \text{and} \qquad b = D_0(t)\,[z_r(t) - z]^{1/3} \tag{2.13}$$

with integration constant $D_0 = D_0(t)$. This asymptotic profile will be used as a time-dependent basis function in a free-boundary element of the discontinuous Galerkin finite-element method.

Conservation of mass for $b > 0$ yields

$$\frac{d}{dt} \int_0^H b(z,t)\, dz = (u\,b)_{z=0} - (u\,b)|_{z=H}, \tag{2.14}$$

and the mass balance is seen to depend on the inflow and outflow at the boundaries.

3 Finite-Element Discretization

We reformulate (2.6) as follows

$$\partial_t b + \partial_z F_b = 0 \qquad \text{and} \qquad \beta\, q + \partial_z F_q = 0 \tag{3.1}$$

with fluxes (F1)

$$F_b = u\,b = (\alpha\, b^2 + \beta\,\sqrt{b}\,q)\,b \qquad \text{and} \qquad F_q = \frac{2}{5}\beta\, b^{5/2} \tag{3.2}$$

or (F2)

$$F_b = u_s b^{3/2} \equiv (\alpha\, b^{3/2} + \beta\, q)\, b^{3/2} \qquad \text{and} \qquad F_q = \frac{2}{5}\beta\, b^{5/2}. \tag{3.3}$$

This formulation is concisely written as

$$\partial_t \tilde{w} + w^\dagger + \partial_z F = 0 \tag{3.4}$$

with variables $\tilde{w} = (b, 0)$ and $w^\dagger = (0, \beta\, q)$, and fluxes $F = (F_b, F_q)$.

3.1 Finite elements

We define a tessellation, $\mathcal{T}_h$, of N_e elements, each denoted by K_k, in the spatial flow domain, $\Omega_f \subseteq \Omega$, with boundary $\partial \Omega_f$:

$$\mathcal{T}_h = \{K_k : \bigcup_{k=1}^{N_e} \bar{K}_k = \bar{\Omega} \text{ and } K_k \cap K_{k'} = \emptyset \text{ if } k \neq k', 1 \leq k, k' \leq N_e\}; \qquad (3.5)$$

here K_k may be a time-dependent free-boundary edge element when it includes the front where the aperture, $b = 0$, and $\bar{K}_k$ denotes the closure of K_k, and such. Element K_k runs from node z_k to node z_{k+1}, and has a length of $|K_k| = z_{k+1} - z_k$. We consider finite-element discretizations of (3.4) with approximations, $w_h = (b_h, q_h)$ to the state vector, (b, q), and basis functions, $v = (v_b, v_q)$, to be introduced. The discretization is such that b_h, q_h, and $v_{b,q}$ belong to the broken space (when K_k is not an edge element)

$$V_h = \{v \,|\, v|_{K_k} \in P^{d_P}(K_k), k = 1, \ldots, N_e\}, \qquad (3.6)$$

in which $P^{d_P}(K_k)$ denotes the space of polynomials in K_k of degree d_P. For edge elements, b_h consists of an asymptotic solution analogous to (2.13).

3.2 Weak formulation

For the moment, we ignore the time dependence of basis and test functions in the edge elements. We multiply (3.1) by test functions, $v = (v_b(z), v_q(z))$, integrate by parts for each individual and isolated element, and then add the contribution from all elements to obtain the following weak formulation

$$\sum_{k=1}^{N_e} \left\{ \int_{K_k} v_b \frac{db_h}{dt} \, dz + [F_b(z_{k+1}^-) \, v_b(z_{k+1}^-) - F_b(z_k^+) \, v_b(z_k^+)] - \int_{K_k} F_b \, \partial_z v_b \, dz \right\} = 0$$

$$\sum_{k=1}^{N_e} \left\{ \int_{K_k} \beta \, v_q \, q_h \, dz + [F_q(z_{k+1}^-) \, v_q(z_{k+1}^-) - F_q(z_k^+) \, v_q(z_k^+)] - \int_{K_k} F_q \, \partial_z v_q \, dz \right\} = 0,$$

$$(3.7)$$

where $v_{b,q}(z_{k+1}^-) = \lim_{z \uparrow z_{k+1}} v_{b,q}(z, t)$ and $v_{b,q}(z_k^+) = \lim_{z \downarrow z_k} v_{b,q}(z, t)$. (We only denote these dependencies explicitly when confusion may arise.) Hence, the fluxes at the faces arising in elements K_k are evaluated inside each element.

Let

$$[[b]] = b_+ - b_- \qquad \text{and} \qquad \bar{b} = (b_+ + b_-)/2 \qquad (3.8)$$

denote the jump and mean in the quantity, b, for example, at z_k with the trace values $b_- = \lim_{z \uparrow z_k} b(z)$ and $b_+ = \lim_{z \downarrow z_k} b(z)$. Consider the flux at a point, z_{k+1}. Because the elements are isolated from one another at this stage, $b_- := b(z_{k+1}^-) \neq$

8

$b(z_{k+1}^+) =: b_+$, and, consequently, the flux $F(z_{k+1}^-) \neq F(z_{k+1}^+)$ in general. The heart of the discontinuous Galerkin numerical method hinges, therefore, on the choice of the numerical flux. To enforce communication and conservation of the fluxes between each element in (3.7), the fluxes $F(z_k^+)$ and $F(z_{k+1}^-)$ at the faces of K_k are replaced by numerical fluxes $\tilde{F}(w_k^-, w_k^+)$ and $\tilde{F}(w_{k+1}^-, w_{k+1}^+)$.

3.3 Flux formulation

The numerical flux, $\tilde{F}(w_-, w_+)$, is chosen to (i) be locally Lipschitz, following Cockburn and Shu (1998), implying that there is a constant, $K \geq 0$, such that

$$|\tilde{F}(w_-, w_+) - F(\bar{u})| \leq K \max(|w_- - \bar{u}|, |w_+ - \bar{u}|)$$

for all w_-, w_+ with $|w_- - \bar{u}|$ and $|w_+ - \bar{u}|$ sufficiently small, (ii) be consistent such that $\tilde{F}(b, b) = F(b)$, (iii) ensure a local determination of q_h in terms of b_h, (iv) reduce to an E-flux in the conservative limit when $\beta = 0$, that is,

$$\int_{b_-}^{b_+} F_b(s; \beta = 0) - \tilde{F}_b(b_-, b_+; \beta = 0)\, ds \geq 0$$

with $F_b(b; \beta = 0) = \alpha\, b^3$, and (v) be L2 stable, as will be shown. Note that the flux is the only way of communication between elements, and that the flux is determined by the values of b_h and q_h immediately left and right of each face.

To ensure positivity of the mean, an upwind scheme is chosen in contrast to the scheme developed by Cockburn and Shu (1998), which turned out to be less or unstable in our application. It is, therefore, necessary to reconsider their L2-stability analysis.

From such an analysis, the following numerical fluxes emerge for F1

$$\tilde{F}_b = \tilde{F}_b(b_\pm, q_\pm) = \begin{cases} \frac{1}{2}\alpha\,(b_+^2 + b_-^2)\,b_- + \beta\,q_+\,b_-\,\sqrt{b_-} & \text{if} \quad \alpha > 0 \quad \& \quad q_+ > 0 \\ \frac{1}{2}\alpha\,(b_+^2 + b_-^2)\,b_- + \beta\,q_+\,b_+\,\sqrt{b_+} & \text{if} \quad \alpha > 0 \quad \& \quad q_+ < 0 \\ \frac{1}{2}\alpha\,(b_+^2 + b_-^2)\,b_+ + \beta\,q_+\,b_-\,\sqrt{b_-} & \text{if} \quad \alpha < 0 \quad \& \quad q_+ > 0 \\ \frac{1}{2}\alpha\,(b_+^2 + b_-^2)\,b_+ + \beta\,q_+\,b_+\,\sqrt{b_+} & \text{if} \quad \alpha < 0 \quad \& \quad q_+ < 0 \end{cases}$$

$$\tilde{F}_q = F_q(b_-).$$

$$(3.9)$$

Alternatively, we also tested for choice F1

$$\tilde{F}_b = \tilde{F}_b(b_\pm, q_\pm) = \begin{cases} \frac{1}{2}\alpha\,(b_+^2 + b_-^2)\,b_- + \beta\,\bar{q}\,b_-\,\sqrt{b_-} & \text{if} \quad \alpha > 0 \quad \& \quad \bar{q} > 0 \\ \frac{1}{2}\alpha\,(b_+^2 + b_-^2)\,b_- + \beta\,\bar{q}\,b_+\,\sqrt{b_+} & \text{if} \quad \alpha > 0 \quad \& \quad \bar{q} < 0 \\ \frac{1}{2}\alpha\,(b_+^2 + b_-^2)\,b_+ + \beta\,\bar{q}\,b_-\,\sqrt{b_-} & \text{if} \quad \alpha < 0 \quad \& \quad \bar{q} > 0 \\ \frac{1}{2}\alpha\,(b_+^2 + b_-^2)\,b_+ + \beta\,\bar{q}\,b_+\,\sqrt{b_+} & \text{if} \quad \alpha < 0 \quad \& \quad \bar{q} < 0 \end{cases} \quad (3.10)$$

$$\tilde{F}_q = \tilde{F}_q(b_\pm) = \bar{F}_q = [F_q(b_-) + F_q(b_+)]/2,$$

and for choice F2

$$\tilde{F}_b = \tilde{F}_b(b_\pm, q_\pm) = \begin{cases} \overline{u_s}\, b_-^{3/2} & \text{if } \overline{u_s} \geq 0 \\ \overline{u_s}\, b_+^{3/2} & \text{if } \overline{u_s} < 0 \end{cases}$$

$$\tilde{F}_q = \tilde{F}_q(b_\pm) = \bar{F}_q = \left[F_q(b_-) + F_q(b_+) \right]/2.$$

(3.11)

For choice F1, we separately use an upwind scheme both for the "convective" wind, $u_{\text{conv}} = \alpha\, b^2$, and the "diffusive" wind component, $u_{\text{diff}} = \beta\, q\, \sqrt{b}$. For choice F2, we use an upwind scheme based on the "scaled" velocity, $u_s = \alpha\, b^{3/2} + \beta\, q$, defined in (3.2). Inspection shows that these fluxes are locally Lipschitz and consistent. The diffusive part of the flux (3.9) for case F1 alternates and is reported to be more stable (Yan and Shu, 2002). The local character follows from the spatial discretization in which q, knowing b at the previous time level, can be solved before it is used in the discrete equations for the aperture, b; see also Appendix A.

Properties (iv) and (v) are proven next. The flux F2 is more compact than flux F1. Readers less interested in further numerical analysis could proceed to the numerics to ensure positivity of the approach and the treatment of the free boundary in §3.5 and further, or to the results in §4.

3.4 L2 stability

L2 stability for the discretized equations follows in an analogy of the L2 stability for the continuous case with α constant. We simply assume that for general $\alpha(z)$ the resulting discretization holds as well. In addition, the case without free boundary is analyzed. To wit, multiply (3.1) times b and q, respectively, sum, and integrate over space and time to obtain:

$$\frac{1}{2} \int_0^H b^2 - b_i^2 \, dz + \int_0^T \int_0^H \beta\, q^2 \, dz\, dt - \int_0^T \int_0^H \left(F_b\, \partial_z b + F_q\, \partial_z q \right) dz\, dt +$$

$$\int_0^T \left(u\, b^2 + F_q\, q \right)_{z=H} - \left(u\, b^2 + F_q\, q \right)_{z=0} \, dt = 0 \iff$$

$$\frac{1}{2} \int_0^H b^2 - b_i^2 \, dz + \int_0^T \int_0^H \beta\, q^2 \, dz\, dt +$$

$$\int_0^T \left(u\, b^2 - \alpha\, b^4/4 \right)_{z=H} - \left(u\, b^2 - \alpha\, b^4/4 \right)_{z=0} \, dt = 0,$$

(3.12)

because

$$F_b\, \partial_z b + F_q\, \partial_z q = \alpha\, b^3 \partial_z b + \beta\, q\, b^{3/2} \partial_z b + (2/5)\, \beta\, b^{5/2}\, \partial_z q = \partial_z \left[\phi(b) + F_q\, q \right]$$

with $\phi(b) = \int_0^b \alpha\, s^3 \, ds = \alpha\, b^4/4$. Note that $b_i(z) = b(z,0)$.

10

The discrete version of L2 stability for F1 and F2 proceeds as follows (*cf.*, Cockburn and Shu, 1998); by adding the weak formulation (3.7) of both equations, we find

$$
b_h(w_h, v_h) = \int_0^T \int_0^H \frac{db_h}{dt}\, v_b + \beta\, v_q\, q_h \, dz\, dt - \int_0^T \sum_{2 \le k \le N_e} (\tilde{F} \cdot [[v_h]])_k \, dt +
$$

$$
\int_0^T (\tilde{F} \cdot v_h^-)_{k=N_e+1} - (\tilde{F} \cdot v_h^+)_{k=1} \, dt - \int_0^T \sum_{1 \le k \le N_e} \int_{K_k} F \cdot \partial_z v_h dz\, dt \tag{3.13}
$$

with $w_h = (b_h, q_h)$ and $v_h = (v_b, v_q)$. As in the continuous case, substitute $v_b = b_h$ and $v_q = q_h$ into (3.13) to obtain:

$$
b_h(w_h, w_h) = \frac{1}{2} \int_0^H (b_h^2 - b_{hi}^2)\, dz + \int_0^T \int_0^H \beta\, q_h^2\, dz\, dt +
$$

$$
\int_0^T \left(\phi(b_h^+) + F_q^+ q_h^+ - \tilde{F} \cdot w_h^+ \right)_{k=1} \, dt - \tag{3.14}
$$

$$
\int_0^T \left(\phi(b_h^-) + F_q^- q_h^- - \tilde{F} \cdot w_h^- \right)_{k=N+1} \, dt + \int_0^T \Theta_{\text{dissipation}}(t)\, dt,
$$

where

$$
\Theta_{\text{dissipation}}(t) = - \sum_{2 \le k \le N} \tilde{F} \cdot [[w_h]] - \sum_{1 \le k \le N} \int_{K_k} F \cdot \partial_z w_h \, dz +
$$

$$
\left[\phi(b_h) + F_q\, q_h \right]_{k=N+1}^- - \left[\phi(b_h) + F_q\, q_h \right]_{k=1}^+. \tag{3.15}
$$

Rewriting

$$
- \sum_{1 \le k \le N} \int_{K_k} F \cdot \partial_z w_h \, dz\, dt = \sum_{2 \le k \le N} [[\phi(b_h) + F_q\, q_h]]_k +
$$

$$
\left[\phi(b_h) + F_q\, q_h \right]_{k=1}^+ - \left[\phi(b_h) + F_q\, q_h \right]_{k=N+1}^- \tag{3.16}
$$

is used to evaluate (3.15) further. Hence, requiring that

$$
\Theta_{\text{dissipation}}(t) = \sum_{2 \le k \le N} \Theta_{\text{dissipation}}^k(t) = \sum_{2 \le k \le N} \left\{ [[\phi(b) + F_q\, q_h]] - \tilde{F} \cdot [[w_h]] \right\}_k
$$

$$
= \sum_{2 \le k \le N} \left\{ [[\phi(b)]] + [[F_q]]\, \bar{q}_h - [[b_h]]\, \tilde{F}_b + \bar{F}_q\, [[q_h]] - [[q_h]]\, \tilde{F}_q \right\}_k > 0 \tag{3.17}
$$

motivates the choice (3.9) and its limits. Reordering the chosen convective flux in the limit $\beta = 0$ produces

$$\lim_{\beta \to 0} \Theta_{\text{dissipation}}^{k}(t) = [[\phi(b_h)]] - [[b_h]] \frac{1}{2} \alpha \, (b_-^2 + b_+^2) \, b_{\pm}$$

$$= \int_{b_-}^{b_+} F_b(s; \beta = 0) - \frac{1}{2} \alpha \, (b_-^2 + b_+^2) \, b_{\pm} \, \mathrm{d}s > 0 \qquad (3.18)$$

for $F_b(b; \beta = 0) = \alpha \, b^3$, when $\alpha \neq 0$ proving property (iv), that the convective part of the flux is an E-flux. The flux, $\tilde{F}_b$, in the diffusive limit is also an upwind flux as it introduces extra stabilizing dissipation because some (graphical) analysis shows that

$$-[[q_h]] \, F_b(b_-) + [[F_q]] \, \bar{q}_h - \beta \, [[b_h]] \, q_+ \left\{ \begin{array}{ll} \sqrt{b_-} \, b_- & \text{if } \bar{q}_h \geq 0 \\ \sqrt{b_+} \, b_+ & \text{if } \bar{q}_h < 0 \end{array} \right\} > 0. \qquad (3.19)$$

For the flux F2, we have been unable to prove L2 stability when $\alpha \neq 0$ and $\beta \neq 0$ because the convective and diffusive parts in general cannot be considered in separation. Nevertheless, in the frictionless limit, $\beta \to 0$, we find

$$\lim_{\beta \to 0} \Theta_{\text{dissipation}}^{k}(t) = [[\phi(b_h)]] - [[b_h]] \frac{1}{2} \alpha \, (b_-^{3/2} + b_+^{3/2}) \, b_{\pm}^{3/2}$$

$$= \int_{b_-}^{b_+} F_b(s; \beta = 0) - \frac{1}{2} \alpha \, (b_-^{3/2} + b_+^{3/2}) \, b_{\pm}^{3/2} \, \mathrm{d}s > 0, \qquad (3.20)$$

while in the diffusive limit, $\alpha \to 0$, (3.19) holds again.

3.5 Time discretization: non-negative mean aperture

The upwind nature of the chosen fluxes is favored to avoid a negative aperture. The idea of a maximum principle (*e.g.*, Morton and Mayers, 1994; Bokhove, 2004) can then be used to estimate a suitable timestep restriction such that the mean aperture in each element remains positive.

Define the mean, $\bar{B}_k$, and fluctuation, $\hat{B}_k$, of b_h in element K_k

$$b_h|_{K_k} = \bar{B}_k + \zeta \, \hat{B}_k \qquad (3.21)$$

with $\zeta \in [-1, 1]$ the reference coordinate in element K_k (see Appendix A). Using the test function $v_b = 1$, we obtain the discrete equation for the mean aperture, $\bar{B}_k$, in element K_k

$$|K_k| \frac{\mathrm{d}\bar{B}_k}{\mathrm{d}t} + \tilde{F}_b(z_{k+1}) - \tilde{F}_b(z_k) = 0, \qquad (3.22)$$

12

where for F1: $\tilde{F}_b = \tilde{F}_b = \langle u \rangle_{conv} b_\pm + \langle u \rangle_{diff} b_\pm$ with $\langle u \rangle_{conv} = \overline{u_{conv}} = \alpha\, b^2$ and

$$\langle u \rangle_{diff} = \begin{cases} \beta\,\bar{q}\,\sqrt{b_-} & \text{if} \quad \bar{q} \geq 0 \\ \beta\,\bar{q}\,\sqrt{b_+} & \text{if} \quad \bar{q} < 0 \end{cases}, \qquad (3.23)$$

and for F2: $\tilde{F}_b = \langle u \rangle_s\, b_\pm^{3/2}$ with $\langle u \rangle_s = \overline{u_s}$. So if $\overline{u_{conv}} \geq 0$ we choose $b_\pm(z_k) = b_-$ and vice versa, and likewise for the diffusive velocity, $\langle u \rangle_{diff}$, and scaled velocity, u_s.

The third-order total variation diminishing Runge-Kutta (RK3) method of Shu and Osher (1989) is used to discretize time (see Appendix A). Given b_k^n at time level, $t = t_n$, then b_k^{n+1} at the next time level, $t = t_{n+1} = t_n + \Delta t$, is found using intermediate stages $b_k^{(1)}$ and $b_k^{(2)}$. Consider the case second order in space for F2 such that at the face z_{k+1}: $b_- = \bar{B}_k + \hat{B}_k$ and $b_+ = \bar{B}_{k+1} - \hat{B}_{k+1}$, with a positive velocity, $\langle u \rangle^n > 0$, and a positive aperture, $b^n > 0$, at time t_n for the first forward Euler intermediate time stage in the RK3 method. We deduce

$$\begin{aligned} \bar{B}_k^{(1)} &= \bar{B}_k^n - \frac{\Delta t}{|K_k|}\, \langle u \rangle_{k+1}^n\, (\bar{B}_k^n + \hat{B}_k^n) + \frac{\Delta t}{|K_k|}\, \langle u \rangle_k^n\, (\bar{B}_{k-1}^n + \hat{B}_{k-1}^n) \\ &\leq \bar{B}_k^n \left(1 - \frac{2\,\Delta t}{|K_k|}\, \langle u \rangle_{k+1}^n \right) + \frac{\Delta t}{|K_k|}\, \langle u \rangle_k^n\, (\bar{B}_{k-1}^n + \hat{B}_{k-1}^n), \end{aligned} \qquad (3.24)$$

since $\bar{B}_k + \hat{B}_k \leq 2\,\bar{B}_k$ if $(b_h)_k > 0$. We can ensure positivity of $\bar{B}_k^{(1)}$ by limiting the time step in (3.24) such that the coefficients of $\bar{B}_k^n$ remain positive (*e.g.*, in the above case)

$$\Delta t_k \leq 0.5\, |K_k|/\langle u \rangle_{k+1}^n. \qquad (3.25)$$

An overall timestep is obtained by taking the smallest timestep resulting from the elements K_k. A similar timestep criterion appears at the other intermediate time stages by taking $\langle u \rangle^{(1)}, \langle u \rangle^{(2)}$ to eventually ensure that $\bar{B}_k^{n+1} > 0$. The same analysis can be made for F1. Because we do not know the values at intermediate stages $t^{(1)}$ and $t^{(2)}$ in advance, it may be necessary to restart the time integration at t_n with a smaller timestep.

In addition, a slope limiter is required such that $\hat{B}_k \pm \bar{B}_k > 0$ at (intermediate) stages. In addition, we used the limiter of Burbeau *et al.* (2001) to limit oscillations around steep gradients. After each completed timestep, closure of the aperture so that $\hat{B}_k \pm \bar{B}_k < 0$ for positive mean $\bar{B}_k$ would indicate that a closing event has emerged.

3.6 Free-boundary elements

In the presented simulations, only one free boundary (point) may be considered with $b = 0$ for $z > z_r(t)$. Consider an underlying fixed mesh of elements and a mesh with flooded elements where $b > 0$. The flooded part of the mesh consists of Eulerian

finite elements coinciding with the fixed mesh for $z < z_k$ and a Eulerian-Lagrangian moving top element with $k = te$ and a fixed bottom node at $z = z_{te}$, and a moving top node with $z_r(t) > z_{te}$.

The aperture in this top element, $k = te$, is expressed in terms of the asymptotic free boundary solution as

$$b_h(z,t) = \frac{4}{3} \bar{B}_{te}(t) \frac{[z_r(t) - z]^{1/3}}{|K_{te}|^{1/3}}, \qquad (3.26)$$

since b_h is approximated by (2.13) and its mean satisfies

$$\bar{B}_{te}(t) = \frac{1}{z_r - z_{te}} \int_{z_{te}}^{z_r} b_h(z,t)\, dz. \qquad (3.27)$$

After substitution in the weak formulation with $v_b = 1$, but now allowing for a time-dependent basis and test functions, mass conservation emerges

$$\frac{d(|K_{te}| \bar{B}_{te})}{dt} - \tilde{F}_b(z_{te}) = 0 \quad \text{and} \quad \frac{dz_r}{dt} = \frac{64\,\beta}{81} \frac{\bar{B}_k^3}{|K_{te}|} \qquad (3.28)$$

with $|K_{te}| = z_r(t) - z_{te}$. Likewise, we can handle a bottom free-boundary element. The discretization of the equation for q remains the same (or can be altered correspondingly), except that the the basis function used for b in a free-boundary element has to be altered.

When the top element becomes too large, for instance, larger than

$$|K_{te}| + 0.6\,|K_{te+1}|_{\text{fixed}},$$

then element K_{te} becomes a regular fixed element and K_{te+1} the new time-dependent top element, see Fig. 2a. Conservation of mass yields $\bar{B}_{te}$ and $\bar{B}_{te+1}$, while $\hat{B}_{te}$ follows by (numerical) projection. When the top element becomes too small, for instance, less than $0.4\,|K_{te}|_{\text{fixed}}$ of the fixed underlying element, then elements K_{te-1} and K_{te} are combined under conservation of mass; see Fig. 2b. A new time-dependent top element, K_{te-1}, emerges with $\bar{B}_{te-1}$, while $\bar{B}_{te}$ becomes void. In principle, closing events emerging in the middle of the domain can be included as well (in the analogy of the drying events in Bokhove, 2004) but were not required in the presented simulations. Furthermore, the timestep criterion for free-boundary elements is adjusted to include the effect of the moving free-boundary node.

4 Results

4.1 Stationary and Traveling-Wave Solutions

Substituting the traveling-wave Ansatz, $b = b(\varphi)$, with $\varphi = (z - ct)$ into (2.6) yields

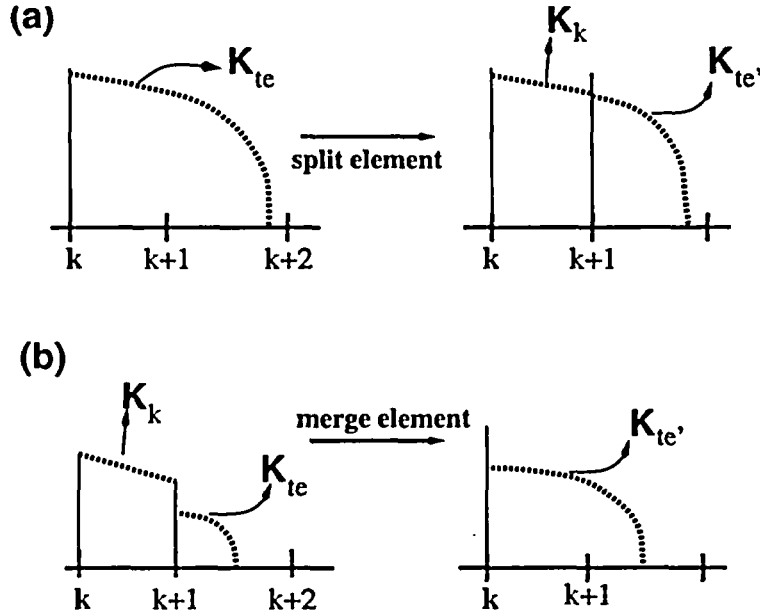$$\beta\,b^3\,b' = \alpha\,b^3 - c\,b - Q = f(b) - Q \qquad (4.1)$$

Figure 2: (a) Splitting and (b) merging of the time-dependent top element with expansion, $b = b_h(z,t) \propto \bar{B}_k(t) [z_\tau(t) - z]^{1/3}$.

with $b' = db/d\varphi$ and the integration constant Q, which equals the flow rate when $c = 0$. Several cases will be considered: stationary solutions with $c = 0$ and $Q \geq 0$, and traveling-wave solutions with $c \neq 0$. For traveling-wave solutions with a free boundary, we must have a finite velocity at the front, and thus $Q = 0$.

4.1.1 Stationary solutions

When $c = 0$, we find

$$\beta\, b^3\, b' = \alpha\, b^3 - Q = f(b) - Q. \tag{4.2}$$

In Fig. 3a, we display $f(b)$ versus b for $\alpha > 0$; with root $b = b_*$ when $f(b)-Q = 0$ while $b, Q > 0$. We note that $b' < 0$ when $f(b) < Q$, so if we start with a value $b = b_B < b_*$ at the bottom, $z = 0$, then the aperture decreases going upward. Otherwise, when $f(b) > Q$, we find $b' > 0$, and the aperture increases. In Fig. 4a, we divide the parameter plane Q–b_B with $b_B > 0$ into an inaccessible region where the aperture closes before the top at $z = H$ and regions where the aperture expands (right of the dash-dotted line) and contracts (between the two indicated lines). Corresponding profiles of z versus $b(z)$ in Fig. 4b for various values of Q illustrate some of the permissable profiles. When the aperture becomes asymptotically small at the top, flow speeds become asymptotically large, implying that the neglected inertia terms are no longer negligible. The profile with a critical flow speed, $u = c = \gamma_c \sqrt{b}$ [cf., (2.8)], implies that $Q = u\, b = \gamma_c\, b_T^{3/2}$, corresponding to the dashed line in Fig. 4b.
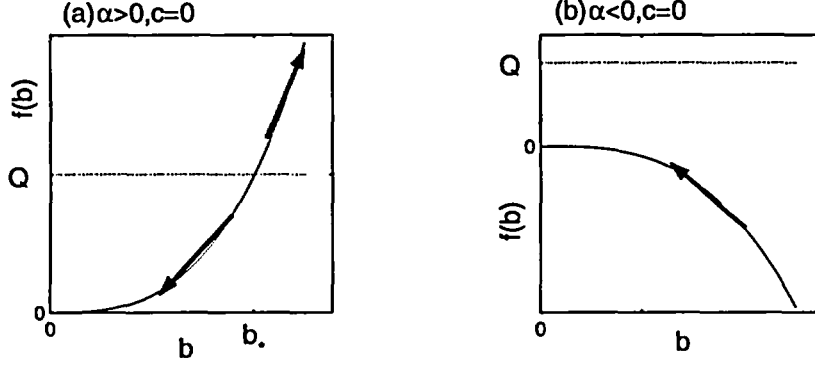
15

Figure 3: The function $f(b)$ versus b for the stationary cases with $c = 0$ and $Q > 0$: (a) for $\alpha > 0$, the dike width contracts for $b < b_*$ and expands when $b > b_*$, and (b) for $\alpha > 0$, the dike width only contracts.

In Fig. 3b, we display $f(b)$ versus b for $\alpha < 0$. We see that when $\alpha < 0$, we always find $b' < 0$ for the relevant cases with $b, Q > 0$. The parameter plane Q-b_B in Fig. 5a indicates that only the contracting profiles emerge, as in Fig. 5b.

In general, the density, ρ_r, of the rock may vary mildly with depth (*e.g.*, approximately linearly),

$$\rho_r = (1 - z/H)\,\rho_0 + \rho_H\,z/H. \tag{4.3}$$

We obtain the same equation (4.2), and the qualitative behavior is the same if the sign of α is definite in the domain. For $\alpha(z) > 0$, we obtain the parameter space Q-b_B, as shown in Fig. 6 with the corresponding depth-versus-aperture-profiles.

Another representative model of the crustal density arises from the Tolbachik volcano region in Kamchatka, Russia, with

$$\rho_r(z) = \begin{cases} 2,400\,kg/m^3 & 26\,km < z < 30\,km \\ 2,600\,kg/m^3 & 22\,km < z < 26\,km \\ 2,800\,kg/m^3 & 0\,km < z < 22\,km \end{cases}. \tag{4.4}$$

So the magma chamber lies at a $30\,km$ depth. Furthermore, the ratio of minimum to maximum principle stress is taken as $\kappa = 0.7$; the viscosity $\mu = 100\,Pa\,s$; the magma density $\rho_m = 2,600\,kg/m^3$; and $\lambda = 10^{-8}m/Pa$. Steady-state solutions of the inertial, elastic equations (see Woods *et al.*, 2004) and the convection-diffusion equations are both displayed in Fig. 7. They are indistinguishable on the scale shown. Hence, the condition of choked flow in the convection-diffusion model seems appropriate here. The steady-state equation for the elastic flow equations (2.4) with $Q = b\,u$ is

$$(b/\lambda - \rho_m\,Q^2/b^2)\,\partial_z b = \partial_z\left(\frac{1}{2}\,b^2/\lambda + \rho_m\,Q^2/b\right) = g\,(\kappa\,\rho_r - \rho_m)\,b - \gamma\,\mu\,Q/b^2. \tag{4.5}$$
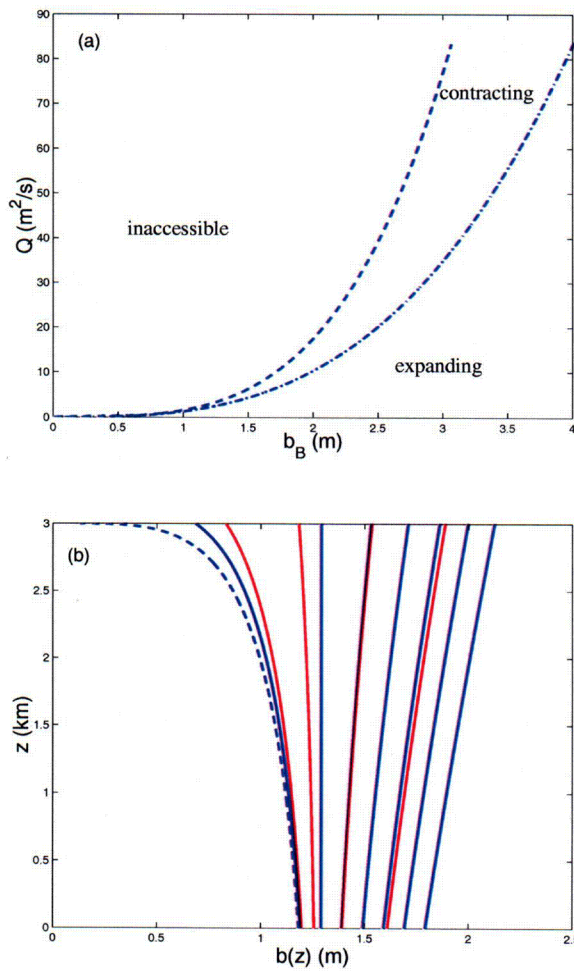
16

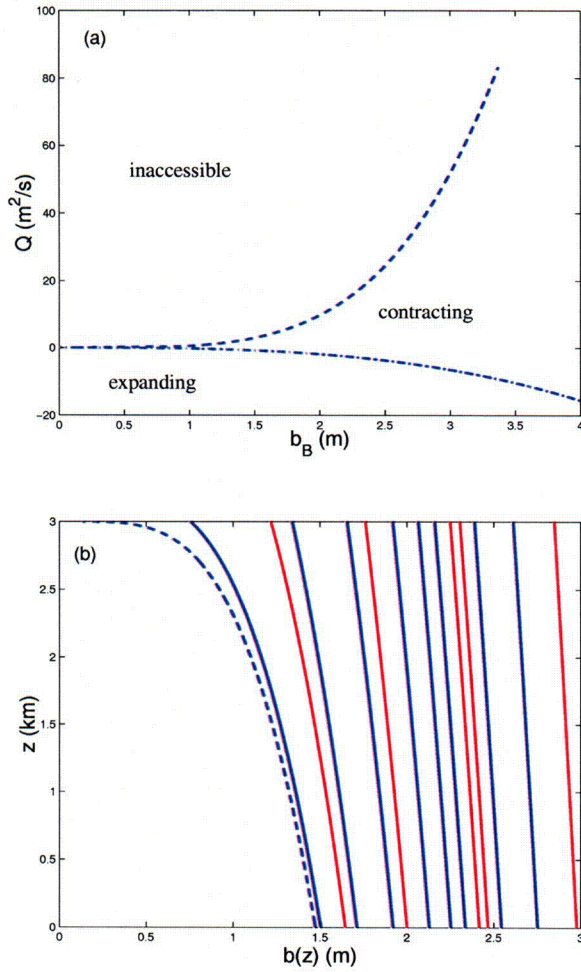Figure 4: Stationary case $\alpha > 0$. (a) The parameter plane Q–b_B with $b_B > 0$ is from left to right divided into an inaccesible, contracting and expanding region. (b) Profiles of the vertical coordinate, z, versus the aperture, $b(z)$, of the latter two regions are displayed. The profile with the dashed line indicates the profile with critical speed at the top for which $u = \gamma_c \sqrt{b}$ and here $b = b_T = 0.1245\,m$ and $Q = 2.7778\,m^2/s$. Parameters are $\alpha = 0.4709, H_0 = 3,000\,m, D_0 = 1\,m, \rho_m = 2,500\,kg/m^3, \rho_r = 2,800\,kg/m^3, \kappa = 0.95, \lambda = 10^{-7}\,m^2\,s^2/kg, \mu = 100\,Pa\,s, g = 9.81\,m/s^2, \gamma = 12,$ and $\gamma_c = 22.77$.
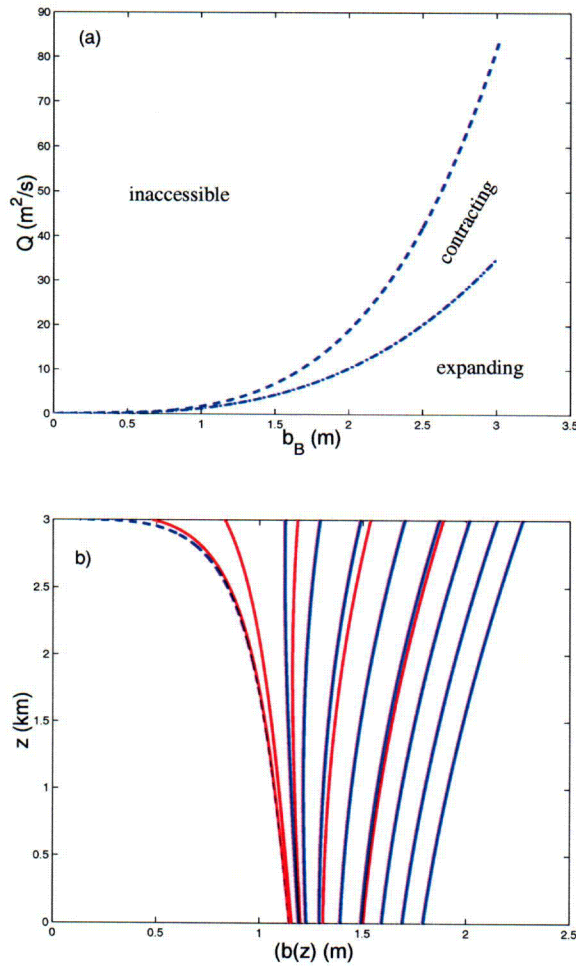
CO2

Figure 5: Stationary case $\alpha < 0$. (a) The parameter plane Q–b_B with $b_B > 0$ is from left to right divided into an inaccessible, contracting and expanding region. (b) Profiles of the vertical coordinate, z, versus the aperture, $b(z)$, of the relevant contracting region are displayed. The profile with the dashed line indicates the profile with critical speed at the top for which $u = \gamma_c \sqrt{b}$ and here $b = b_T = 0.1245\,m$ and $Q = 2.7778\,m^2/s$. The parameters are $\alpha = -0.0883$, $H_0 = 3,000\,m$, $D_0 = 1\,m$, $\rho_m = 2,500\,kg/m^3$, $\rho_r = 2,600\,kg/m^3$, $\kappa = 0.95$, $\lambda = 10^{-7}\,m^2\,s^2/kg$, $\mu = 100\,Pa\,s$, $g = 9.81\,m/s^2$, $\gamma = 12$, and $\gamma_c = 22.77$.

C03

Figure 6: Stationary case with $\alpha = \alpha(z)$. (a) The parameter plane Q–b_B with $b_B > 0$ is from left to right divided into a choked, contracting and expanding region. (b) Profiles of the vertical coordinate, z, versus the aperture, $b(z)$, of the latter two regions are displayed. The profile with critical speed at the top corresponds with the dashed line and $b_T = 0.1245\,m$. Parameter values are $H_0 = 3{,}000\,m$, $D_0 = 1\,m$, $\rho_m = 2{,}500\,kg/m^3$, $\rho_0 = 2{,}800\,kg/m^3$, $\rho_H = 2{,}800\,kg/m^3$, $\kappa = 0.95$, $\lambda = 10^{-7}\,m^2\,s^2/kg$, $\mu = 100\,Pa\,s$, $g = 9.81\,m/s^2$, and $\gamma = 12$.
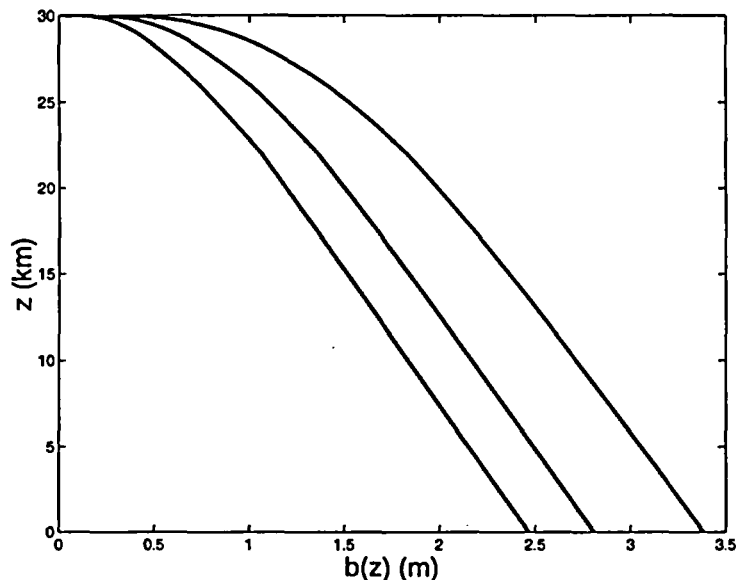
Figure 7: Stationary solutions for the three flow rates $Q = b\,u = 0.289, 1.766, 9.96\,m^2/s$ from left to right for both the elastic-flow and convection-diffusion models. Note that these two solutions per flow rate are indistinguishable in the scale shown. Parameter values are assumed to model the Tolbachik volcano region in Kamchatka, Russia.

For choked flow, $\partial_z b$ is infinite, and $u \approx \gamma_c \sqrt{b} \propto \sqrt{H - z}$ near the top. We used this asymptotic shape of the profile of u to scale the finite difference grid to obtain a numerical solution.

4.1.2 Traveling-wave solutions

When $c \neq 0$, traveling-wave solutions emerge. We consider first the most relevant cases with constant $\alpha > 0$. In Fig. 8, we display $f(b)$ versus b and denoted the roots of $f(b) - Q = 0$ by b_0, b_1, or b_*. Note that Q is no longer the flow rate. Four cases emerge with (a) $c > 0, Q = 0$, (b) $c < 0, Q > 0$, (c) $c > 0, Q < 0$, and (d) $c > 0, Q > 0$. We don't consider (sub)cases in which b may become zero and $Q \neq 0$, and hence exclude the case with $c, Q < 0$. The cases (b), (c), and (d) with $\alpha > 0$ correspond to the cases (b') $c > 0, Q < 0$, (c') $c < 0, Q > 0$, and (d') $c < 0, Q < 0$ for constant $\alpha < 0$ when we reverse the sign of b'. Hence, we do not consider cases with $\alpha < 0$ separately.

For choked flow at the top boundary, the boundary condition for traveling waves is $Q = \gamma_c a_T^{3/2} - c a_T$. So for traveling-wave free-boundary solutions this choked-flow condition yields $c = \gamma_c a_T^{3/2} > 0$.

Solutions with fronts exist for $Q \neq 0$ with finite discharge and infinite velocity at the front. The exception is the case $Q = 0$ for which the velocity at the front is finite
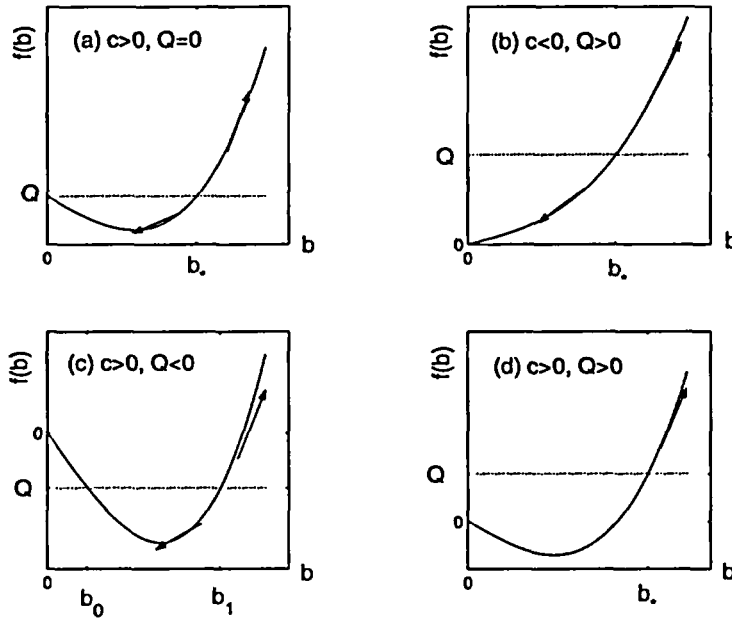
Figure 8: $f(b)$ versus b for the four traveling wave cases considered with $\alpha > 0$: (a) for $c > 0, Q = 0$ there is one root b_* and two situations $b < b_*$ where $b' < 0$, and $b > b_*$ where $b' > 0$; (b) for $c < 0, Q > 0$ there is one root b_* and two situations $b < b_*$ where $b' < 0$, and $b > b_*$ where $b' > 0$; (c) for $c > 0, Q < 0$ there are two roots b_0, b_1 and three situations with $b < b_0$ where $b' > 0$, $b_0 < b < b_1$ where $b' < 0$, and $b > b_1$ where $b' > 0$; and (d) for $c > 0, Q > 0$ there is one root b_* and two situations $b < b_*$ where $b' < 0$, and $b > b_*$ where $b' > 0$. Arrows indicate whether $b' > 0$ or $b' < 0$ and are not added when $b \downarrow 0$ for $Q \neq 0$ as these cases are excluded.
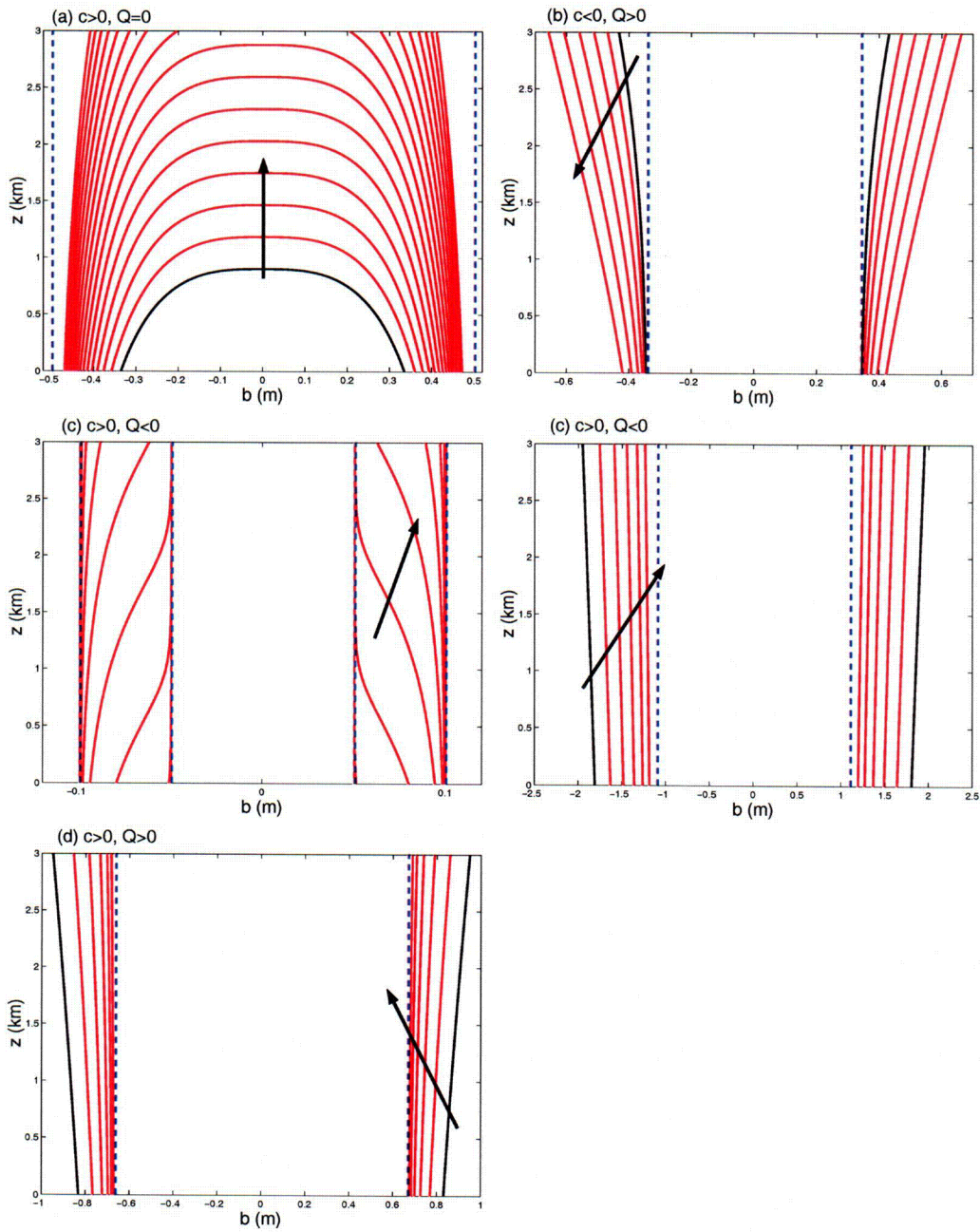
21

Figure 9: Profiles of the depth, z, versus the aperture, $b(z,t)$, for the traveling wave solutions with $\alpha > 0$. Arrows indicate the propagation direction of the wave.

C05

Run	Location	Type	$\tilde{F}_b$	$\tilde{F}_q$
Fig. 10	$z = 0$	Dirichlet	$\tilde{F}_b(b_\pm, q_+)$	$F_q(b_-)$
	$z = H$	choked	$\gamma_c b_-^{3/2}$	$F_q(b_-)$
Fig. 11	$z = 0$	Dirichlet	$\tilde{F}_b(b_\pm, q_+)$	$F_q(b_-)$
	$z = H$	Dirichlet	$\tilde{F}_b(b_\pm, q_-)$	$F_q(b_+)$
Fig. 12	$z = 0$	Dirichlet	$\tilde{F}_b(b_\pm, q_+)$	$F_q(b_-)$
	$z = z_r(t)$	free	0	0
	$z = H$	Dirichlet	$\tilde{F}_b(b_\pm, q_-)$	$F_q(b_+)$
Fig. 14	$z = 0$	Dirichlet	$\tilde{F}_b(b_\pm, q_+)$	$F_q(b_-)$
	$z = z_r(t)$	free	0	0
	$z = H$	choked	$\gamma_c b_-^{3/2}$	$F_q(b_-)$
Fig. 16	$z = 0$	Dirichlet	$\tilde{F}_b(b_\pm, q_+)$	$F_q(b_-)$
	$z = z_r(t)$	free	0	0
	$z = H$	choked	$\gamma_c b_-^{3/2}$	$F_q(b_-)$

Table 2: The boundary conditions are provided at $z = 0$; and $z = z_r(t)$ (free boundary), $z = H$ (fixed) or $z = H(t)$ (dome growth), whichever is applicable, for the five runs presented for flux formulation F1 (3.9). The free-boundary conditions are valid provided $0 < z_r(t) < H$.

and the exact solution is

$$\frac{\beta}{\alpha}\left[b - \sqrt{c/\alpha}\, \text{arctanh}(\sqrt{\alpha}\, b/\sqrt{c})\right] = z - z_r(t) = z - z_{r0} - ct \qquad (4.6)$$

with integration constant z_{r0} the position of the front at $t = 0$.

The profiles for the depth, z, versus the aperture, $b(z, t)$, for the traveling-wave cases are shown in Fig. 9 for cases (a) $b' < 0$ and $Q = 0$; (b) $b' > 0$; (c) $b' < 0, b_0 < b < b_1$ and $b' > 0, b > b_1$; and (d) $b' > 0$, corresponding to the cases in Fig. 8. The arrows indicate the direction or time propagation of the wave, and the dashed lines indicate the constant aperture limits corresponding to the roots in the cases (b) b_*, (c) b_0, b_1 with $b_0 < b_1$, and (d) b_*.

4.2 Numerical Verification

To verify the algorithm and numerical implementation, a comparison is made between the numerical solutions of the partial differential equations with a mixture of (time-dependent) Dirichlet, choked-flow, and free-boundary conditions, and high(er) resolution exact or numerical solutions of the stationary and traveling-wave solutions governed by the relevant ordinary differential equation. For the full system, we use
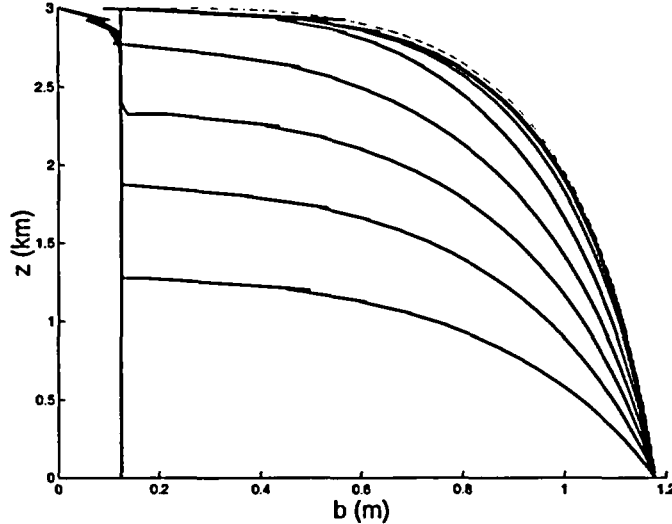
23

Figure 10: The evolution of the aperture, $b(z,t)$, as function of depth, z, is shown for the numerical solution (solid lines) at times $0, 1.8, \ldots, 45\,min$ (dimensionless $t = 0.1, \ldots, 2.5$). The final, nearly stationary state as a high-resolution (fourth order Runge Kutta space discretization and 10 times higher resolution) numerical solution of the relevant ordinary differential equation is displayed as a dashed line. The Dirichlet condition at $z = 0$ and initial conditions are $b_B = 1.1774489332$ and $b(z,0) = 0.1244834652$. At the top, the choked flow is imposed. $\alpha = 0.4709$, $\beta = 1.0$, and $\gamma_c = 22.7683991532$. Forty equidistant elements are used.

second-order accuracy in space and choose the timestep sufficiently small, while, for the ordinary differential equations, we use a fourth-order Runge-Kutta spatial discretization and at least a tenfold higher resolution. Only the results of formulation F1 are shown because the results of the two formulations are similar. In each case, the total number of underlying fixed elements is stated. The boundary conditions used in the five presented simulations are summarized in Table 2. When nothing is mentioned, the flux rule as it stands in (3.9) is implemented.

To determine the spatial accuracy, the L_2-norm of the error has been used (and approximated by taking the mean values in each element)

$$L_2 = \sqrt{\frac{1}{H_{\text{wet}}} \int_0^{H_{\text{wet}}} (b_{\text{numerical}} - b_{\text{exact}})^2 \, \mathrm{d}z}, \tag{4.7}$$

and the L_∞ norm, the maximum absolute difference between the numerical and the "exact" solution with H_{wet} the inundated, open part of the domain.

We considered stationary solution and two traveling-wave solutions, corresponding to Fig. 4 for (a) $c = 0, \alpha > 0$; and Fig. 9 for (a) $c > 0, Q = 0$ and (c) $c > 0, Q < 0$ with $b < b_*$ and $b_0 < b < b_1$.

24

	$N = 20$ Error	$N = 40$ Error	Order	$N = 80$ Error	Order	$N = 160$ Error	Order
L_2	0.0376041	0.020769	0.86	0.011052	0.91	0.005590	0.98
L_∞	0.037604	0.16191	0.38	0.12085	0.42	0.08668	0.48

Table 3: L_2 and L_∞ errors as function of resolution and the spatial order of accuracy for the stationary case with $c = 0, \alpha > 0$. Polynomial order $d_P = 1$. Solutions are considered at dimensionless time $t = 2.5$.
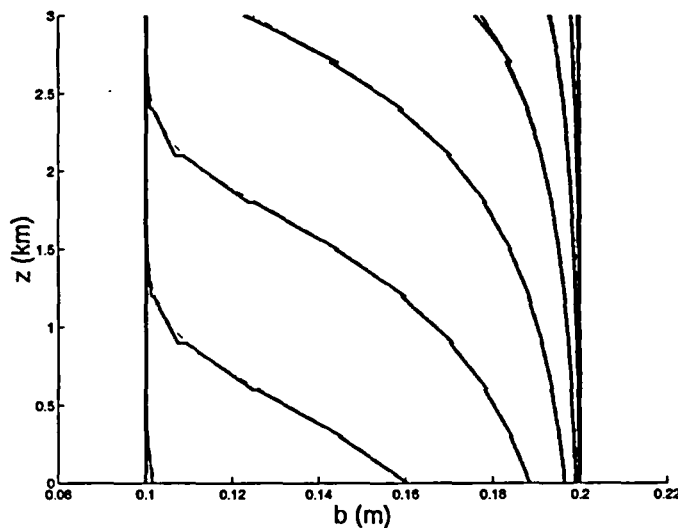

Figure 11: The evolution of the aperture, $b(z,t)$, as function of depth, z, for the numerical solution (solid lines) at times $0, 3.6, \ldots, 36\,hr$ (dimensionless $t = 0, 0.012, \ldots, 0.12$). The fourth profile at $18\,hrs$ in the middle of the graph is used to determine the L_2 and L_∞ errors. The traveling-wave solution is a high-resolution (fourth order Runge Kutta space discretization and approximately 10 times higher resolution) numerical solution of the relevant ordinary differential equation. For each time, this solution displayed as a dashed line. The Dirichlet conditions are time dependent and given by the traveling-wave solution with dimensionless $c = 32.9616$ and $Q = -28.2528$. $\alpha = 4.7088$ and $\beta = 1.0$. Ten equidistant elements are used.

25

	$N = 10$ Error	$N = 20$ Error	Order	$N = 40$ Error	Order	$N = 80$ Error	Order
L_2	0.0067878	0.0022502	1.5929	0.0007432	1.5982	0.0002381	1.6419
L_∞	0.0140886	0.0049057	1.5220	0.0016545	1.5680	0.0005139	1.6870

Table 4: L_2 and L_∞ errors as functions of resolution and the spatial order of accuracy for the traveling-wave case with $c > 0, Q < 0, b_0 < b < b_1$. Polynomial order $d_P = 1$. Solutions are considered at dimensionless time $t = 0.06$.

The exact stationary solution with Dirichlet and choked-flow boundary conditions, displayed in Fig. 4b with the dashed line, was considered first. The sequence of numerical solutions approaching this state are displayed in Fig. 10. Table 3 shows that the spatial accuracy reduces to order 1 for the L_2-error and order 0.5 for the L_∞-error in the stationary case because of the steep gradient and the choked-flow condition, both at $z = H$. In Fig. 10, this discrepancy is observed at $z = H = 3\,km$, where the largest pointwise error occurs. Such a reduction of order is also observed in solutions with shocks or discontinuities. The exact and numerical traveling-wave solution is shown in Fig. 11. Table 4 shows that the spatial accuracy is approximately $1.5 - 1.64$ for the traveling-wave case, as opposed to the expected, formal second-order accuracy.

The exact and numerical traveling-wave solution with a free boundary propagating in the domain is provided in Fig. 12. The numerical solution uses the free-boundary strategy explained in §3.6. The numerical solution corresponds relatively well with the exact solution. The L_2-error has an order of 1.6, while the L_∞-error behaves poorly and fluctuates heavily. The actual time of splitting an element in relation to the measurement time makes the latter error a poor indicator of the order of convergence. Oscillations in the speed of the frontal position shown in Fig. 13 are caused by the element-splitting procedure.

4.3 Validation

The validity of the mathematical model and numerical modeling is illustrated by presenting numerical solutions of magma flow through an opening elastic dike from a magma chamber with a fixed pressure until the dike reaches the surface. The subsequent growth of a lava dome or pile implies that the overpressure of the magma chamber reduces. Once the lava pile reaches a critical height, failure causes immediate removal of the pile on the slow time scale considered, whence the overpressure in the magma chamber is suddenly increased again.
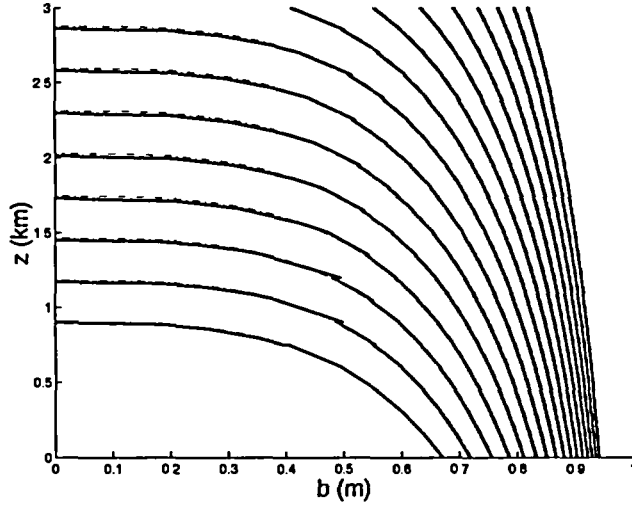
Figure 12: The evolution of the aperture, $b(z,t)$, as function of depth, z, for the numerical solution (solid lines) at times $0, 3.6, \ldots, 54\,min$ (dimensionless $t = 0, 0.2, \ldots, 3$). The fifth profile at $14.4\,min$ in the middle of the picture is used to determine the L_2 and L_∞ errors. The traveling-wave solution is provided by the exact solution for $Q = 0$ (dashed lines). The Dirichlet conditions are time dependent and provided by the traveling-wave solution with dimensionless $c = \alpha = 0.4709$, $\beta = 1$. Twenty equidistant underlying regular elements are used, of which only a fraction is used with one time-dependent free-boundary element when the aperture is only open, $b > 0$, in part of the domain.

	$N = 10$ $\frac{\text{Error}}{10^{-4}}$	$N = 20$ $\frac{\text{Error}}{10^{-4}}$	Order	$N = 40$ $\frac{\text{Error}}{10^{-4}}$	Order	$N = 80$ $\frac{\text{Error}}{10^{-4}}$	Order	$N = 160$ $\frac{\text{Error}}{10^{-4}}$	Order
L_2	127.7914	51.171	1.32	17.467	1.55	4.591	1.93	1.490	1.62
L_∞	181.7607	108.029	0.75	40.409	1.42	10.364	1.96	7.276	0.51

Table 5: L_2 and L_∞ errors as functions of resolution and the spatial order of accuracy for the traveling-wave case with $c > 0, Q = 0$. In the interior, the polynomial order is $d_P = 1$, and at the free boundary, a fractional basis function is used. Solutions are considered at dimensionless time $t = 0.8$.
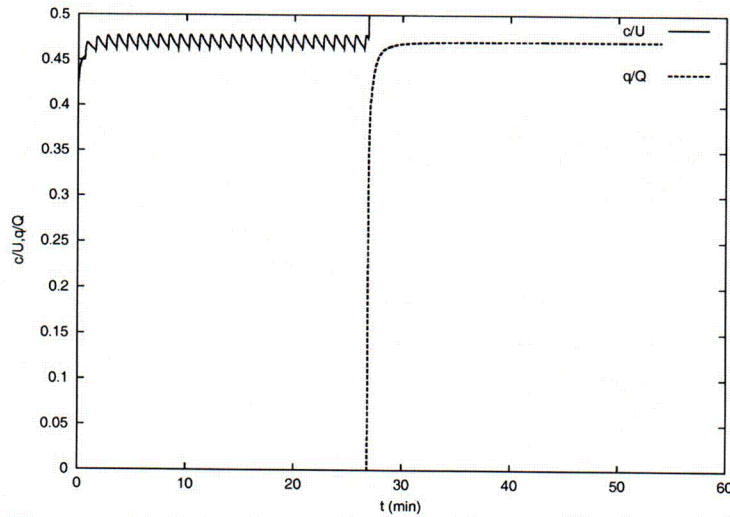
Figure 13: The speed of the front, dz_r/dt, till $t \approx 27\,min$ and the discharge, $q = u\,d$, are displayed at the end of the dike after $t \approx 27\,min$. This speed should be $c/U = 0.4709$ (with dimensional $U = 2.778\,m/s$) and the discharge $q/Q = 0.4709$ ($Q = 2.778\,m^2/s$). The oscillations in the frontal speed clearly demarcate the element-splitting process; there are 40 fixed elements.

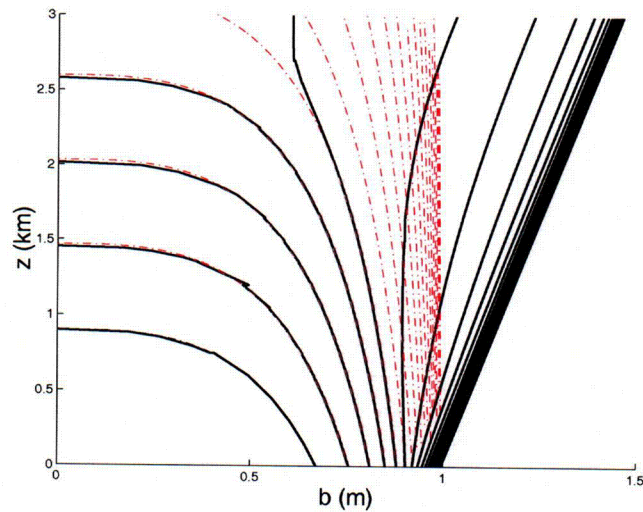
Figure 14: The same simulation as in Fig. 12 but after the magma reaches the exit; the flow at the exit is choked. Profiles at times $0, 7.2\,min, \ldots, 2.4\,hrs$ (dimensionless $t = 0, 0.4, \ldots, 8$). The dashed lines represent the traveling-wave solution with corresponding exact solution before the magma meets the exit. This exact solution is used to determine the Dirichlet condition at $z = 0$ for all times.
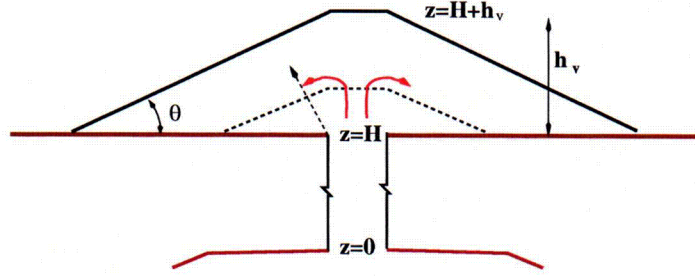
28

Figure 15: The cross-sectional area of the lava dome is assumed to consist of the two triangles shown. The elongated dike is considered to have constant width as approximation to a very thin dike with an elliptical cross section in a horizontal plane. The dome height, $h_v(t)$, depends on the eruption area and the inclination angle, θ.

4.4 Lava dome growth and collapse

We consider the growth of a lava dome of modest height as a consequence of a lava eruption at the Earth's surface. As long as the ratio of dome height, h_v, versus the depth of the magma chamber, $H = 10\,km$, is small, the convection-diffusion equation is appropriate. Otherwise, the edifice load has to be taken into account, as in Pinel and Jaupart (2000). Parameter values include $\mu = 1,000\,Pa\,s$, $\lambda = 10^{-7}$, $\kappa = 0.95$, $\rho_m = 2,500\,kg/m^3$, $\rho_r = 2,800\,kg/m^3$, and roughly mimick estimates for the Soufrière Hills Volcano in Montserrat (Melnik and Sparks, 1999). The overpressure in the absence of a lava dome is approximately $10\,MPa$ against a lithostatic pressure of approximately $\rho_r\,g\,H = 275\,MPa$.

During its growth, a simplified shape of the dome, which cross-sectional area consists of two triangles, will be assumed. The shape of this dome is an approximation of a very elongated, solid elliptical cone excluding the volume of the dike through the cone, see Fig. 15. Hence, we deduce that, for a dome of height $h_v(t)$ and angle of incline θ, the cross-sectional area, $O = O(t)$, is

$$O(t) = h_v\left(w_{1/2} + h_v/\tan\theta\right) \approx h_v\left(a_T/2 + h_v/\tan\theta\right) \qquad (4.8)$$

with the half-width of the dike in the dome $w_{1/2} \approx a(H, t)/2 = a_T(t)/2$. This area is the cumulation in time of the discharge of lava at the growing top of the dike and starts at time t_0 when the dike breaks through the surface at $z = H$ when $h_v(t_0) = 0$. The $w_{1/2}$-factor is included to avoid an infinite growth speed when $h_v \downarrow 0$. Alternatively, one could fill an area of fixed width so that the dome shape is rectangular. The shape of the dome is simply chosen to illustrate the leading-order dynamics and has no further significance. Lava flow will again start at some time less than t_0 from the magma chamber at $z = 0$ following the exact solution (4.6). Upon breakthrough at
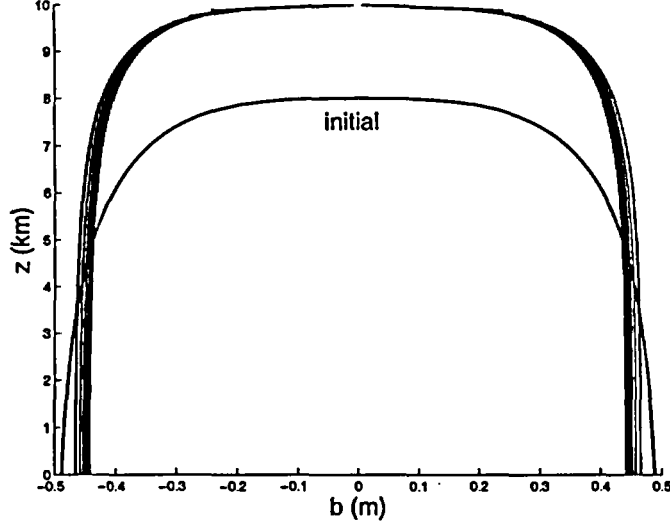
29

Figure 16: Profiles of the evolution approximately every 67 hrs. After approximately five hours the dike reaches the surface, and the eruption reaches a periodic cycle. In total, 80 elements are used.

time t_0 the speed dz_r/dt will change abruptly from the speed of the lava front to the growth speed of the dome height, dh_v/dt,

$$\frac{dh_v}{dt} \approx \frac{2\,u_T(t)\,b_T(t)}{b_T + 4\,h_v/\tan\theta},$$

(4.9)

because $h_v(t_0) - H = h_v(t_0) = 0$. This relationship follows from relating the area growth to the discharge rate at the top of the dike: $dO(t)/dt = u_T(t)\,b(t)$ with the critical velocity $u_T(t) = u(z = H, t)$ at the top, $z = H$, of the dike and likewise for width b_T. In addition, we neglected $\partial b/\partial t|_{z=H}$.

The bottom boundary condition is Dirichlet and follows from expression (4.6) minus the additional pressure increase because of the dome growth. After breakthrough, the width at the magma chamber decreases following relation (2.2) because the absolute pressure in the host rock increases as the dome grows in height.

After the dome growth starts, the dike width decreases as the constant magma overpressure needs to overcome a larger lithostatic pressure of the host rock and lava dome combined, see Fig. 16. In the initial phase, the dike propagates to the surface with a speed of $0.1308\,m/s$ to break through after approximately five hours. After breakthrough, the discharge in Fig. 17 becomes periodic as the dome collapses and disappears instantly (on the slow time scale modeled) after the dome height reaches a critical height chosen to be $h_v = 50\,m$. The periodicity observed is approximately $100\,hrs$.
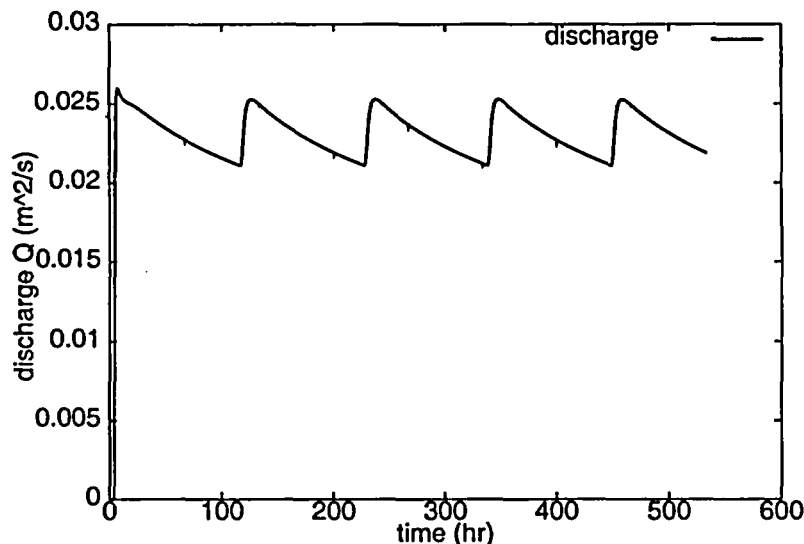
Figure 17: The discharge at the dike tip (per unit length along the dike) versus time shows the eruption reaches a periodic cycle when the dome collapses every time it reaches a critical height, here chosen to be $h_v = 50\,m$.

5 Conclusion and Discussion

The flow of incompressible magma through a dike has been investigated in a model with leading-order coupling between the elastic rock walls and the magma flow. The resulting convection-diffusion model admitted various stationary and traveling-wave solutions, and more complex numerical solutions were found with a new discretization method. The stationary and traveling-wave solutions were used as building blocks to understand the evolving flows and end-states in geophysical applications. More detailed information was obtained by performing simulations for a variety of time-dependent boundary conditions using the developed local discontinuous Galerkin finite-element method. The numerical method displayed a convergence of order 1.6 for smooth solutions in the L_2-norm also for a free-boundary solutions which were treated with a special arbitrary Lagrangian-Eulerian time-dependent element. For flows with steep gradients, the L_2-norm reduced to order one because a slope limiter was needed to ensure stability (see Burbeau et al., 2001). The L_∞-error showed a convergence of 1.6 for a smooth solution without free boundary, and order 0.5 was reached in the free-boundary case and the case where steep gradients emerged.

The numerical finite-element method developed can readily be extended to asymmetric flows in the two-dimensional dike plane and can then be considered in complicated geometries, which can arise because of heterogeneities in the rock or dike intersection with a subsurface tunnel. For the two-dimensional extension of the convection-diffusion model, it may be advisable to use an implicit Crank-Nicolson time discretization. The latter will permit shorter time steps and enhance stability, in which case a slope limiter is probably no longer required (cf., Yan & Shu, 2002).

31

The formulation of the proper in- and outflow boundary conditions in averaged models with a simplified elastic response of the host rock remains an outstanding question. Nevertheless, the critical flow condition at the exit gave satisfactory results. In particular, steady-state solutions of the convection-diffusion model with the critical flow condition at the surface were nearly indistinguishable with steady-state solutions of the elastic model in which the inertia terms are not neglected. Solution of this elastic model, further geophysical applications of the current model for steady-state conditions and including the compressible effects of viscous, bubbly magma, are found in Woods et al. (2004).

Presumably, improved conditions follow from further consideration of the feedback between the dynamics in the dike and the response of the magma chamber and the coupling with the erupted flows above and over the Earth's surface.

References

Bokhove, O. (2004) Flooding and drying in discontinuous Galerkin finite-element discretizations of shallow-water equations. Part 1: one dimension. Accepted for publication *J. of Sci. Comp.*

Burbeau, A., Sagaut, P., and Bruneau, Ch.-H. (2001) A problem-independent limiter for high-order Runge-Kutta Discontinuous Galerkin methods. *J. Comp. Phys.* **169**, 111–150.

Cockburn, B., and Shu, C.-W. (1998) The local discontinuous Galerkin method for time-dependent convection-diffusion systems. *Siam. J. Numer. Anal.* **135**, 2240–2463.

Melnik, O, and Sparks, R.S.J. (1999) Nonlinear dynamics of lava dome extrusion. *Nature* **402**, 37–41.

Morton, K.W., and Mayers, D.F. (1994) Numerical solution of partial differential equations. Cambridge University Press.

Pinel, P., and Jaupart, C. (2000) The effect of edifice load on magma ascent beneath a volcano. In: *Causes and consequences of eruptions of andesite volcanoes.* Eds. P. Francis, J. Neuberg and R.S.J. Sparks. *Phil. Trans. R. Soc. London. A* **358**, 1515–1532.

Shu, C.-W., and Osher, S. (1989) Efficient implementation of essentially non-oscillatory shock-capturing schemes II. *J. Comp. Phys.* **83**, 32-78.

Yan, J, and Shu, C.-W. (2002) Local discontinuous Gakerkin methods for partial differential equations with higher order derivatives. ICASE report, NASA/CR-2-2-211959, 16 pp.

Whitham, G.B. (1974) *Linear and nonlinear waves.* John Wiley, 636 pp.

Woods, A.W., Bokhove, O., Boer de, A., and Hill, B.E. (2004) Compressible magma flow in a two-dimensional elastic-walled conduit. Submitted to *Earth and Planetary Sci. Lett.*, 18 pp.

A Discontinuous Galerkin Finite-Element Method

A.1 Geometry and polynomial basis functions

In one dimension, the bounded interval $\Omega := [0, H] \subset \mathbb{R}$ is partitioned by $N_e + 1$ "regular" faces (points in one dimension) $\mathcal{E} := \{z_k\}_{k=0}^{N_e}$ and into N_e "regular" elements. It is convenient to introduce a reference element in one dimension, $\hat{K} = [-1, 1]$, and define the mapping $F_K : \mathbb{R} \to \mathbb{R}$ between the reference element, $\hat{K}$, and element K_k as follows: $z = F_{K_k}(\zeta) = \sum_{m=1}^{2} z_{k,m} \chi_m(\zeta) = \hat{z}_k + |K_k| \zeta/2$, where the $z_{k,1} = z_{k,L}$ and $z_{k,2} = z_{k,R}$ are the left and right end points of element $K_k = (z_{k,L}, z_{k,R}) = (z_k, z_{k+1})$. The shape functions are $\chi_1(\zeta) = (1-\zeta)/2$, $\chi_2(\zeta) = (1+\zeta)/2$. Note that $\hat{z}_{k,1} = (z_{k,L} + z_{k,R})/2$, $|K_k|(t) = (z_{k,R} - z_{k,L})$. In the basis element $\hat{K}$, we define basis functions

$$\hat{\varphi}_0(\zeta) = 1 \quad \text{and} \quad \hat{\varphi}_m(\zeta) = \zeta^m \quad \text{for} \quad m = 1, \ldots, d_P. \tag{A.1}$$

Finally we relate the local basis functions in $\hat{K}$ to the basis functions in K_k as follows:

$$\hat{\varphi}_n(\zeta) = \hat{\varphi}_n[F_{K_k}^{-1}(z, t)] = \varphi_{n,k}(z, t) \quad \text{for} \quad n = 0, \ldots, d_P. \tag{A.2}$$

In principle, elements can be time dependent by allowing the nodes to move in time. We distinguish fixed interior elements where $b > 0$ and edge elements where $b = 0$ at one of the nodes.

To unify notation, for F1, we have $w = (b, q)$, and for F2, take $w = (b, q = u)$. The vector (b, q) in both F1 and F2 and test functions, v, are approximated in each interior element, K_k, by their polynomial approximations (for time-independent elements), (b_h, q_h) and $v_{b,q}$, as follows:

$$b_h(z, t) = \sum_{m=0}^{d_P} \hat{B}_m(K_k, t) \, \psi_m(z, t), \qquad v_{b,q}(z) = \sum_{m=0}^{d_P} \hat{v}_m(K_k) \, \psi_m(z, t) \tag{A.3}$$

with polynomial basis functions $\psi_m(z, t) \in P^{d_P}(K_k)$. These are chosen such that

$$\hat{B}_0 = \bar{B}(K_k, t) = \int_{K_k} b(z, t) \, dz/|K_k| \quad \text{and}$$

$$\psi_{m,k}(z) = \left\{ \begin{array}{ll} 1 & \text{if } m = 0 \\ \varphi_{m,k}(z, t) - \int_{K_k} \varphi_{m,k}(z, t) \, dz/|K_k| & \text{if } m \geq 1 \end{array} \right\}.$$

Likewise, we approximate q with q_h.

A.2 Weak formulation and finite-element discretization

Taking $d_P = 1$ in (A.3), we approximate b_h by a mean and a slope

$$b_h(z, t) = \bar{B}_k + \hat{B}_k\,\psi_{1,k}(z, t) \quad \text{and} \quad v_h(z) = \bar{W}_k + \hat{W}_k\,\psi_{1,k}(z, t) \qquad (A.4)$$

with $\bar{B}_k = \bar{B}(K_k, t)$, and such, and likewise for q_h. We now restrict to the case, where the nodes remain fixed. Since $\bar{W}_k$ and $\hat{W}_k$ are arbitrary, we obtain the following equations for the mean and fluctuating part after substituting (A.4) into (3.7) for formulation F1 and F2:

$$|K_k|\frac{d\bar{B}_k}{dt} + \tilde{F}_b(z_{k+1}) - \tilde{F}_b(z_k) = 0$$

$$\frac{|K_k|}{3}\frac{d\hat{B}_k}{dt} + [\tilde{F}_b(z_{k+1}) + \tilde{F}_b(z_k)] - \int_{-1}^{1} F_b(b_h, q_h)\,d\zeta = 0$$

$$\beta\,|K_k|\,\bar{Q}_k + \tilde{F}_q(z_{k+1}) - \tilde{F}_q(z_k) = 0 \qquad (A.5)$$

$$\beta\,\frac{|K_k|}{3}\,\hat{Q}_k + [\tilde{F}_q(z_{k+1}) + \tilde{F}_q(z_k)] - \int_{-1}^{1} F_q(b_h, q_h)\,d\zeta = 0.$$

The integrals are approximated with a third-order Gauss quadrature rule.

A.3 Time integration

We write (A.5) as a system of ordinary differential and algebraic equations

$$\frac{db}{dt} = G_b(b, q) \quad \text{and} \quad q = G_q(b) \qquad (A.6)$$

with $b = (\bar{B}, \hat{B})$ the state vector of unknown coefficients of the basis functions, and $q = (\bar{Q}, \hat{Q})$. We can then use the third-order Runge-Kutta method of Shu and Osher (1989), for example, to discretize (A.6) in time, and obtain

$$q^n = G_q(b^n) \qquad b^{(1)} = b^n + \Delta t\,G_b(b^n, q^n)$$

$$q^{(1)} = G_q(b^{(1)}) \qquad b^{(2)} = \Big[3\,b^n + b^{(1)} + \Delta t\,G_b(b^{(1)}, q^{(1)})\Big]/4 \qquad (A.7)$$

$$q^{(2)} = G_q(b^{(2)}) \qquad b^{n+1} = \Big[b^n + 2\,b^{(2)} + 2\,\Delta t\,G_b(b^{(2)}, q^{(2)})\Big]/3.$$

Note that we can solve for b and q in an explicit manner because the new (intermediate) stage of q can always be found from the new (intermediate) stage of b before commencing the time update.

B List of Symbols

$\alpha = \alpha(z)$, dimensionless coefficient for advective term
a, long semi-axis of elliptical cross section
$b = b(z, t)$, aperture, and short semi-axis of elliptical cross section

34

$b^{(0)}, b^{(1)}, b^{(2)}$, and such, consecutive coefficients in series expansion of $b = b(z,t)$

$b_B(t)$, boundary value of $b(z,t)$ at $z = 0$

$b_T(t)$, boundary value of $b(z,t)$ at $z = H$

$\bar{B}_k, \hat{B}_k$, numerical coefficients in finite element discretization of variable, $b(z,t)$

$\bar{B}_{te}$, mean coefficient of top (free boundary) element

β, dimensionless diffusive coefficient

c_e, elastic wave speed

c, traveling wave speed

d_P, degree of the polynomial used in the finite element approximation

D_0, length scale of aperture b

ϵ, small parameter

$\eta = (z_\tau - z)/\epsilon$, stretched coordinate at the free boundary

f function used in determining the stationary and traveling-wave solutions

F, flux

F_b, flux of the aperture equation

F_q, flux for diffusive variable q

g, accelaration of gravity

G, rigidity

G_b, G_q, righthand sides in numerical discretization

γ, frictional coefficient

γ_c, coefficient in dimensionless elastic wave speed

h_v, height of lava dome

H, length of domain

H_0, length scale of H

K_k, element k

K_{te}, top finite element at free boundary

$\bar{K}_k$, closure of element, K_k

κ, anisotropy parameter, ratio between horizontal and vertical stresses

k, k', finite element index

λ, elasticity of the rock

L_2, L_∞, error measures

μ, viscosity of magma

N_e, number of finite elements

ν, Poisson's ratio

Ω, Ω_f, domain and spatial flow domain, respectively

$\partial\Omega_f$, boundary of spatial flow domain

$p = p(z,t)$, pressure of magma

$p_r = p_r(z)$, pressure in the host rock

$p_B = p_B(t)$, pressure in the magma chamber at the bottom

p_T, ambient pressure

$\varphi = z - ct$, traveling wave coordinate

$\hat{\phi}_n, \phi_m$, polynomials outside and inside the reference element

q, diffusive aid variable in numerical formulation

Q, Q_f, integration constants of the flux expressed as area per second

$\bar{Q}_k, \hat{Q}_k$, numerical coefficients in numerical approximation of variable q

ρ_m, constant density of magma

ρ_r, constant density of the host rock

ρ_0, ρ_H, constant densities

t, time

τ, stretched or slow time coordinate

T_0, time scale

$\mathcal{T}_h$, tesselation

$u = u(z, t)$, the vertical velocity of the magma averaged over the cross section of the dike

$u_r = u_r(t)$, frontal velocity at $z = z_r(t)$

$u_{\text{diff}}, u_{\text{conv}}$, diffusive and convective part of the advective velocity

u_T, velocity at top of dike

v, v_b, v_q, test function, general, and for variables b and q, respectively

w_h, b_h, q_h, numerical approximation of $w = (b, q)$

z, vertical coordinate

$z_r = z_r(t)$, position of free boundary where $b \to 0$.

U.S. NUCLEAR REGULATORY COMMISSION

RELEASE TO PUBLISH UNCLASSIFIED NRC CONTRACTOR
SPEECHES, PAPERS, AND JOURNAL ARTICLES
(Please type or print)

1. TITLE (State in full as it appears on the speech, paper, or journal article)
Magma Flow through Elastic-Walled Dikes

2. AUTHOR(s)
O. Bokhove, A.W. Woods, and A. de Boer

3. NAME OF CONFERENCE, LOCATION, AND DATE(s)

4. NAME OF PUBLICATION
Theoretical and Computational Fluid Dynamics

5. NAME AND ADDRESS OF THE PUBLISHER

Springer-Verlag GmbH & Co. KG
Herstellung
Andrea Kübler
Tiergartenstr. 17
69121 Heidelberg, Germany

TELEPHONE NUMBER OF THE PUBLISHER

Phone: 062214878448
Fax: 062214878688
E-mail: kuebler@springer.de

6. CONTRACTOR NAME AND COMPLETE MAILING ADDRESS (Include ZIP code)

Brittain Hill
Center for Nuclear Waste Regulatory Analyses
6220 Culebra Road
San Antonio, Texas 78238

TELEPHONE NUMBER OF THE CONTRACTOR

210.522.6087

7. CERTIFICATION
(ANSWER ALL QUESTIONS)

YES	NO	
	✔	**A. COPYRIGHTED MATERIAL** — Does this speech, paper, or journal article contain copyrighted material? If yes, attach a letter of release from the source that holds the copyright.
	✔	**B. PATENT CLEARANCE** — Does this speech, paper, or journal article require patent clearance? If yes, the NRC Patent Counsel must signify clearance by signing below.

NRC PATENT COUNSEL *(Type or Print Name)*	SIGNATURE	DATE

YES	NO	
✔		**C. REFERENCE AVAILABILITY** — Is all material referenced in this speech, paper, or journal article available to the public either through a public library, the Government Printing Office, the National Technical Information Service, or the NRC Public Document Room? If no, list below the specific availability of each referenced document.

	SPECIFIC AVAILABILITY

YES	NO	
✔		**D. METRIC UNIT CONVERSION** — Does this speech, paper, or journal article contain measurement and weight values? If yes, all must be converted to the International System of Units, followed by the English units in brackets, pursuant to the NRC Policy Statement implementing the Omnibus Trade and Competitiveness Act of 1988, Executive Order 12770, July 25, 1991.

8. AUTHORIZATION

The signatures of the NRC project manager and the contractor official certify that the NRC contractor speech, paper, or journal article is authorized by NRC, that it has undergone appropriate peer review for technical content and for material that might compromise commercial proprietary rights, and that it does not contain classified, sensitive unclassified, or nonpublic information. (NRC MD 3.9, Part II(A)(1)(d))

A. CONTRACTOR AUTHORIZING OFFICIAL *(Type or print name)* **Budhi Sagar**	SIGNATURE	DATE 6/10/04

B. NRC RESPONSIBLE PROJECT MANAGER *(Type or print name)*	OFFICE/DIVISION	MAIL STOP

TELEPHONE NUMBER	E-MAIL I.D.	Did you place the speech, paper, or journal article in the PDR? YES _____ NO _____

SIGNATURE	DATE

U.S. NUCLEAR REGULATORY COMMISSION

RELEASE TO PUBLISH UNCLASSIFIED NRC CONTRACTOR
SPEECHES, PAPERS, AND JOURNAL ARTICLES
(Please type or print)

1. TITLE (State in full as it appears on the speech, paper, or journal article)
Magma Flow through Elastic-Walled Dikes

2. AUTHOR(s)
O. Bokhove, A.W. Woods, and A. de Boer

3. NAME OF CONFERENCE, LOCATION, AND DATE(s)

4. NAME OF PUBLICATION
Theoretical and Computational Fluid Dynamics

5. NAME AND ADDRESS OF THE PUBLISHER

Springer-Verlag GmbH & Co. KG
Herstellung
Andrea Kübler
Tiergartenstr. 17
69121 Heidelberg, Germany

TELEPHONE NUMBER OF THE PUBLISHER

Phone: 062214878448
Fax: 062214878688
E-mail: kuebler@springer.de

6. CONTRACTOR NAME AND COMPLETE MAILING ADDRESS (Include ZIP code)

Brittain Hill
Center for Nuclear Waste Regulatory Analyses
6220 Culebra Road
San Antonio, Texas 78238

TELEPHONE NUMBER OF THE CONTRACTOR

210.522.6087

7. CERTIFICATION
(ANSWER ALL QUESTIONS)

YES	NO	
	✔	**A. COPYRIGHTED MATERIAL** — Does this speech, paper, or journal article contain copyrighted material? If yes, attach a letter of release from the source that holds the copyright.
	✔	**B. PATENT CLEARANCE** — Does this speech, paper, or journal article require patent clearance? If yes, the NRC Patent Counsel must signify clearance by signing below.

NRC PATENT COUNSEL (Type or Print Name)	SIGNATURE	DATE

YES	NO	
✔		**C. REFERENCE AVAILABILITY** — Is all material referenced in this speech, paper, or journal article available to the public either through a public library, the Government Printing Office, the National Technical Information Service, or the NRC Public Document Room? If no, list below the specific availability of each referenced document.

SPECIFIC AVAILABILITY

YES	NO	
✔		**D. METRIC UNIT CONVERSION** — Does this speech, paper, or journal article contain measurement and weight values? If yes, all must be converted to the International System of Units, followed by the English units in brackets, pursuant to the NRC Policy Statement implementing the Omnibus Trade and Competitiveness Act of 1988, Executive Order 12770, July 25, 1991.

8. AUTHORIZATION

The signatures of the NRC project manager and the contractor official certify that the NRC contractor speech, paper, or journal article is authorized by NRC, that it has undergone appropriate peer review for technical content and for material that might compromise commercial proprietary rights, and that it does not contain classified, sensitive unclassified, or nonpublic information. (NRC MD 3.9, Part II(A)(1)(d))

A. CONTRACTOR AUTHORIZING OFFICIAL (Type or print name) **Budhi Sagar**	SIGNATURE	DATE 6/10/04

B. NRC RESPONSIBLE PROJECT MANAGER (Type or print name)	OFFICE/DIVISION	MAIL STOP

TELEPHONE NUMBER	E-MAIL I.D.	Did you place the speech, paper, or journal article in the PDR? YES _____ NO _____

SIGNATURE	DATE

U.S. NUCLEAR REGULATORY COMMISSION

RELEASE TO PUBLISH UNCLASSIFIED NRC CONTRACTOR
SPEECHES, PAPERS, AND JOURNAL ARTICLES
(Please type or print)

1. TITLE (State in full as it appears on the speech, paper, or journal article)
Magma Flow through Elastic-Walled Dikes

2. AUTHOR(s)
O. Bokhove, A.W. Woods, and A. de Boer

3. NAME OF CONFERENCE, LOCATION, AND DATE(s)

4. NAME OF PUBLICATION
Theoretical and Computational Fluid Dynamics

5. NAME AND ADDRESS OF THE PUBLISHER

Springer-Verlag GmbH & Co. KG
Herstellung
Andrea Kübler
Tiergartenstr. 17
69121 Heidelberg, Germany

TELEPHONE NUMBER OF THE PUBLISHER

Phone: 062214878448
Fax: 062214878688
E-mail: kuebler@springer.de

6. CONTRACTOR NAME AND COMPLETE MAILING ADDRESS (Include ZIP code)

Brittain Hill
Center for Nuclear Waste Regulatory Analyses
6220 Culebra Road
San Antonio, Texas 78238

TELEPHONE NUMBER OF THE CONTRACTOR

210.522.6087

7. CERTIFICATION
(ANSWER ALL QUESTIONS)

YES	NO	
	✔	**A. COPYRIGHTED MATERIAL** – Does this speech, paper, or journal article contain copyrighted material? If yes, attach a letter of release from the source that holds the copyright.
	✔	**B. PATENT CLEARANCE** – Does this speech, paper, or journal article require patent clearance? If yes, the NRC Patent Counsel must signify clearance by signing below.

NRC PATENT COUNSEL (Type or Print Name)	SIGNATURE	DATE

YES	NO	
✔		**C. REFERENCE AVAILABILITY** – Is all material referenced in this speech, paper, or journal article available to the public either through a public library, the Government Printing Office, the National Technical Information Service, or the NRC Public Document Room? If no, list below the specific availability of each referenced document.

SPECIFIC AVAILABILITY

YES	NO	
✔		**D. METRIC UNIT CONVERSION** – Does this speech, paper, or journal article contain measurement and weight values? If yes, all must be converted to the International System of Units, followed by the English units in brackets, pursuant to the NRC Policy Statement implementing the Omnibus Trade and Competitiveness Act of 1988, Executive Order 12770, July 25, 1991.

8. AUTHORIZATION

The signatures of the NRC project manager and the contractor official certify that the NRC contractor speech, paper, or journal article is authorized by NRC, that it has undergone appropriate peer review for technical content and for material that might compromise commercial proprietary rights, and that it does not contain classified, sensitive unclassified, or nonpublic information. (NRC MD 3.9, Part II(A)(1)(d))

A. CONTRACTOR AUTHORIZING OFFICIAL (Type or print name)	SIGNATURE	DATE
Budhi Sagar		6/10/04

B. NRC RESPONSIBLE PROJECT MANAGER (Type or print name)	OFFICE/DIVISION	MAIL STOP

TELEPHONE NUMBER	E-MAIL I.D.		
		Did you place the speech, paper, or journal article in the PDR? YES _____ NO _____	

SIGNATURE	DATE